

The least-squares analysis of the moments of the charge distribution in the mean-field models

Toshio Suzuki¹

Research Center for Electron Photon Science, Tohoku University,
Sendai 982-0826, Japan

The n th moment of the charge distribution is composed of not only the $m(\leq n)$ th moments of the point proton distribution, but also the $m(\leq (n-2))$ th ones of the point neutron distribution. The experimental value observed through electromagnetic interaction makes it possible to investigate the point proton and neutron distributions together. Comparing the moments of the charge distribution in the mean-field models with experimental values from electron scattering, each value of the related moments of the point proton and neutron distributions is estimated in ^{40}Ca , ^{48}Ca and ^{208}Pb by the least-squares analysis(LSA). The LSA determines the value of the m th moment uniquely as a result of the sum rule for the coefficients of the regression equations. The investigation of the high-order moments like the sixth one provides detailed information on the nuclear models. To obtain experimental values of such moments from electron scattering, however, a new way to analyze cross sections is required, instead of the conventional Fourier-Bessel- and sum-of-Gaussians-methods.

1 Introduction

Electron scattering is one of the best probes to investigate the point proton distribution in nuclei among various methods[1]. Since the electromagnetic interaction and the reaction mechanism are well understood theoretically[2], the scattering process is completely separated from assumptions on the nuclear structure. Moreover, the relationship between the nuclear charge distribution and the point proton one is well defined[3]. The nuclear charge density is composed of the proton and neutron charge densities, but is dominated by the former. The neutron density is less than about 1% of the total density, and its radial dependence oscillates to yield the integrated charge to be zero, as shown in Fig. 1. As a result, electron scattering has been used as a probe to explore the point proton distribution throughout the periodic table[4], and has not been employed so far to investigate the point neutron distribution, which is another fundamental quantity to dominate nuclear structure. The neutron distribution has been studied with other probes mainly through strong interaction which is dealt with rather model-dependently, compared with electromagnetic interaction[1].

Recently, it has been pointed out that the neutron charge density plays an appreciable role in the n th($n \geq 4$) moments of the nuclear charge distribution[5], because at the nuclear surface, contribution from the neutron charge density to the total one becomes non-negligible, as expected from Fig. 1. The n th moment of the nuclear charge distribution is shown to include the contribution from the $m(\leq (n-2))$ th moment of the point neutron distribution, in addition to the $m(\leq n)$ th moment of the point proton distribution[5]. This fact implies that both the point proton and the point neutron distribution are explored together, using the same experimental data through well-known electromagnetic interaction. It is not possible, however, to extract the neutron contribution model-independently, because the n th($n \geq 4$) moment has several components whose values are not determined uniquely by experiment. Strictly speaking, even the second moment of the charge density is not simply given by the point proton distribution[6].

¹kt.suzuki2th@gmail.com

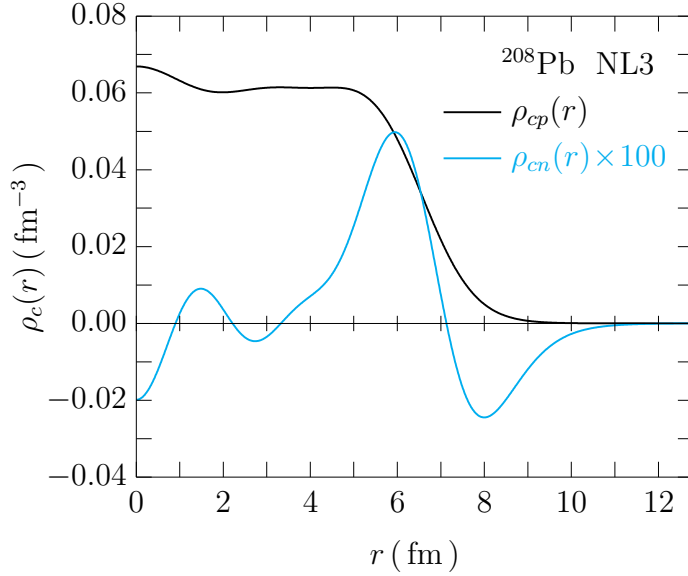


Figure 1: The charge density($\rho_c(r)$) of ^{208}Pb as a function of the nuclear coordinate(r) calculated by the relativistic mean-field model(NL3), taking into account the finite size of the nucleon. The proton($\rho_{cp}(r)$) and the neutron($\rho_{cn}(r)$) charge densities are shown by the black and blue curves, respectively. The former is almost the same as the total charge density, $\rho_c(r)$. For details, see the text.

Hence, in order to estimate the value of each component separately, Ref.[6] has employed the least-squares analysis(LSA) for the values of the moments predicted in the mean-field(MF) models, which have been widely used to describe the fundamental properties of nuclei for long time[7].

The LSA used to analyze the moments is as follows. First, many MF models are arbitrarily chosen within the same model-framework like the relativistic MF(RMF)-framework, or the Skyrme-type MF(SMF)-framework in the literature[8, 9]. In Ref.[6], two sets composed of the 11 RMF-models and the 9 SMF-ones were prepared. Next, the n th moment and its component, for example, the fourth moment(Q_c^4) of the charge distribution and the second moment of the point neutron distribution(R_n^2) in ^{48}Ca , are calculated using each model. Third, a pair of the two calculated values are plotted on the $(R_n^2 - Q_c^4)$ -plane as an element, $(R_{n,i}^2, Q_{c,i}^4)$, by the model named i in the set. Fourth, the regression equation of the least-squares line(LSL) for the elements is obtained, together with the standard deviation and the correlation coefficient between two quantities. Finally, the value of the component R_n^2 is determined by the cross point(LSL-value) of the LSL with the line of the experimental value of Q_c^4 observed through electron scattering. Thus, the LSA is not a way to determine the experimental value of each component, but to estimate the value accepted in the used model-framework. Actually, Ref.[6] has estimated the values of R_n allowed in the RMF- and SMF-frameworks for ^{40}Ca , ^{48}Ca and ^{208}Pb within 1% error², together with the ones of the root mean-square-radius(msr), R_p , of the point proton distribution³, using the experimental data available at present[4, 10].

The present paper is an extension of Ref.[6], where the components of Q_c^4 in the MF models are explored. In this paper, the sixth moments of the charge distribution(H_c^6) will be investigated. As far as the author knows, the structure of H_c^6 will be discussed for the first time in nuclear physics. Among the components of H_c^6 , the values of R_n^2 and the fourth moment of the

²Note that the estimation of the error in Ref.[6] is different from that in the present paper mentioned later.

³Note that the second moment is frequently called the mean square radius, and its root is rms in the literature.

point neutron distribution(Q_n^4), and those of R_p^2 , the fourth moment(Q_p^4) and the sixth moment of the point proton distribution(H_p^6) will be estimated in ^{40}Ca , ^{48}Ca and ^{208}Pb . The well defined LSLs between those moments and H_c^6 will be obtained with the small standard deviation and the correlation coefficients almost equal to 1. Unfortunately, however, there is no reliable experimental values of H_c^6 yet. It will be shown in Appendix that the Fourier-Bessel(FB)- and sum-of-Gaussians(SOG)-coefficients listed in Ref.[4] is not sufficient for deducing the experimental values of H_c^6 . Hence, the obtained values by the FB- and SOG-methods will be called the ‘experimental ones’, but used for reference only in the discussions.

In this paper, the structure of LSL will be also discussed in detail so as to develop an understanding of the present analysis on H_c^6 and of previous one on Q_c^4 [6]. The LSL shows the linear relationship between the n th moment like H_c^6 and its one component. Hence, it may not be obvious whether or not the LSL-values can be used in the original expression of the n th moment described as a function of the several components. It will be shown that each value of the components in the function is uniquely given by the corresponding LSL-value in the model-framework, and its function reproduces the experimental value of the n th moment. This fact will be proved as a result of the sum rule for the slope of the LSLs with respect to the n th moment.

In the next section, the relativistic and non-relativistic expressions of H_c^6 will be derived explicitly, following Ref.[5], where the equation of the n th moment has been given. The non-relativistic expression of the sixth moment is derived, in the same way as for the second and the fourth moment[6], by the Foldy-Wouthuysen transformation of the four-component framework to the two-component one. In §3, the values of H_c^6 will be estimated by taking a few MF-models as examples, so that the contribution of each components in H_c^6 would be understood quantitatively. It will be shown that the contributions of the neutrons to H_c^6 are increased more than to Q_c^4 . In §4, the LSA of the relationship between various components and H_c^6 will be performed in the same way as in Ref.[6] for Q_c^4 . Since the experimental values of H_c^6 are uncertain, the values obtained from the SOG-method will be used for reference. Following the results of §4 and those of Ref.[6], the structure of LSL will be discussed in §5. The final section will be devoted to a brief summary.

2 The relativistic and non-relativistic expressions of the sixth moment

Neglecting the center of mass correction, the sixth moment of the nuclear charge density is described as

$$H_c^6 = \langle r^6 \rangle_c = \sum_{\tau=p,n} \langle r^6 \rangle_{c\tau}, \quad (1)$$

where $\langle r^6 \rangle_{c\tau}$ is given by

$$\langle r^6 \rangle_{c\tau} = \frac{1}{Z} \int d^3r r^6 \rho_{c\tau}(r), \quad (2)$$

with the proton charge density, $\rho_{cp}(r)$, and the neutron charge density, $\rho_{cn}(r)$, satisfying $\int d^3r \rho_{cp}(r) = Z$, the number of the protons in the nucleus, and $\int d^3r \rho_{cn}(r) = 0$, respectively. Following Refs.[5, 6], it is convenient to use the Fourier component of $\rho_{c\tau}(r)$ for calculations of H_c^6 ,

$$\tilde{\rho}_{c\tau}(q) = \int d^3r \exp(i\mathbf{q} \cdot \mathbf{r}) \rho_{c\tau}(r) = \int d^3r j_0(qr) \rho_{c\tau}(r). \quad (3)$$

Then, Eq.(2) is written as

$$\langle r^6 \rangle_{c\tau} = \frac{1}{Z} (-\nabla_{\mathbf{q}}^2)^3 (\tilde{\rho}_{G\tau}(q) + \tilde{\rho}_{F\tau}(q))|_{\mathbf{q}=0}, \quad (4)$$

where

$$\tilde{\rho}_{G\tau}(q) = \int d^3r j_0(qr) G_{E\tau}(q^2) \rho_{\tau}(r), \quad \tilde{\rho}_{F\tau}(q) = \int d^3r j_0(qr) F_{2\tau}(q^2) W_{\tau}(r). \quad (5)$$

In the above equations, $G_{E\tau}(q^2)$ and $F_{2\tau}(q^2)$ denote the Sachs and Pauli form factors of the nucleon, and $\rho_{\tau}(r)$ and $W_{\tau}(r)$ stand for the relativistic point nucleon distribution and the spin-orbit density, respectively. The explicit forms of the nucleon form factors are provided in Ref.[6] as,

$$G_{Ep}(q^2) = \frac{1}{(1 + r_p^2 q^2/12)^2}, \quad F_{2p} = \frac{G_{Ep}(q^2)}{1 + q^2/4M^2}, \quad (6)$$

$$G_{En}(q^2) = \frac{1}{(1 + r_+^2 q^2/12)^2} - \frac{1}{(1 + r_-^2 q^2/12)^2}, \quad F_{2n} = \frac{G_{Ep}(q^2) - G_{En}(q^2)/\mu_n}{1 + q^2/4M^2},$$

with

$$r_p = 0.877 \text{ fm}, \quad r_{\pm}^2 = (0.830)^2 \mp 0.058 \text{ fm}^2.$$

The relativistic expressions of $\rho_{\tau}(r)$ and $W_{\tau}(r)$ are written in the MF models as[5, 6],

$$\rho_{\tau}(r) = \sum_{\alpha \in \tau} \frac{2j_{\alpha} + 1}{4\pi r^2} (G_{\alpha}^2 + F_{\alpha}^2), \quad (7)$$

$$W_{\tau}(r) = \frac{\mu_{\tau}}{M} \sum_{\alpha \in \tau} \frac{2j_{\alpha} + 1}{4\pi r^2} \frac{d}{dr} \left(\frac{M - M^*(r)}{M} G_{\alpha} F_{\alpha} + \frac{\kappa_{\alpha} + 1}{2Mr} G_{\alpha}^2 - \frac{\kappa_{\alpha} - 1}{2Mr} F_{\alpha}^2 \right), \quad (8)$$

where j_{α} denotes the total angular momentum of a single-particle, $\kappa_{\alpha} = (-1)^{j_{\alpha} - \ell_{\alpha} + 1/2} (j_{\alpha} + 1/2)$, and ℓ_{α} the orbital angular momentum. The function $G_{\alpha}(r)$ and $F_{\alpha}(r)$ stand for the radial parts of the large and small components of the single-particle wave function, respectively, with the normalization,

$$\int_0^{\infty} dr (G_{\alpha}^2 + F_{\alpha}^2) = 1. \quad (9)$$

The spin-orbit density is a relativistic correction due to the anomalous magnetic moment of the nucleon, μ_{τ} ($\mu_p = 1.793$, $\mu_n = -1.913$), and its role is enhanced by the effective nucleon mass, $M^*(r) = M + V_{\sigma}(r)$, $V_{\sigma}(r)$ being the σ meson-exchange potential which behaves in the same way as the nucleon mass, M , in the equation of motion. The value of M^* depends on the relativistic MF models, but is nearly equal to $0.6M$. Eq.(7) satisfies $\int d^3r \rho_{\tau}(r) = Z$ for $\tau = p$, and N , the number of the neutrons in the nucleus, for $\tau = n$, respectively, while Eq.(8) does $\int d^3r W_{\tau}(r) = 0$, as it should.

Using Eq.(6) to (8), Eq.(4) is calculated in the same ways as in Ref.[5],

$$\begin{aligned} \frac{1}{Z} (-\nabla_{\mathbf{q}}^2)^3 \tilde{\rho}_{Gp}(q)|_{\mathbf{q}=0} &= \langle r^6 \rangle_p + 7r_p^2 \langle r^4 \rangle_p + \frac{35}{2} r_p^4 \langle r^2 \rangle_p + \frac{35}{3} r_p^6, \\ \frac{1}{N} (-\nabla_{\mathbf{q}}^2)^3 \tilde{\rho}_{Gn}(q)|_{\mathbf{q}=0} &= 7(r_+^2 - r_-^2) \langle r^4 \rangle_n + \frac{35}{2} (r_+^4 - r_-^4) \langle r^2 \rangle_n + \frac{35}{3} (r_+^6 - r_-^6), \\ \frac{1}{Z} (-\nabla_{\mathbf{q}}^2)^3 \tilde{\rho}_{Fp}(q)|_{\mathbf{q}=0} &= \langle r^6 \rangle_{Wp} + 7 \left(r_p^2 + \frac{3}{2M^2} \right) \langle r^4 \rangle_{Wp} + \frac{35}{2} \left(r_p^4 + \frac{2r_p^2}{M^2} + \frac{3}{M^4} \right) \langle r^2 \rangle_{Wp}, \\ \frac{1}{N} (-\nabla_{\mathbf{q}}^2)^3 \tilde{\rho}_{Fn}(q)|_{\mathbf{q}=0} &= \langle r^6 \rangle_{Wn} + 7 \left(s_2 + \frac{3}{2M^2} \right) \langle r^4 \rangle_{Wn} + \frac{35}{2} \left(s_4 + \frac{2}{M^2} s_2 + \frac{3}{M^4} \right) \langle r^2 \rangle_{Wn}, \\ & \quad (s_k = r_p^k - (r_+^k - r_-^k)/\mu_n). \end{aligned}$$

In the right-hand sides of the above equations, we have used the same notations as in Ref.[5]. Finally, the relativistic expression of the sixth moment is described in terms of H_{cn}^6 and H_{cp}^6 of the proton and neutron charge distributions expressed, respectively, as

$$H_c^6 = H_{cp}^6 - H_{cn}^6, \quad (10)$$

$$H_{cp}^6 = \langle r^6 \rangle_{cp} = H_p^6 + H_{4p} + H_{2p} + H_{W_p} + \frac{35}{3}r_p^6, \quad (11)$$

$$H_{cn}^6 = -\langle r^6 \rangle_{cn} = H_{4n} + H_{2n} + H_{W_n} - \frac{35}{3}(r_+^6 - r_-^6)\frac{N}{Z}, \quad (12)$$

where the components of H_{cn}^6 and H_{cp}^6 are given by

$$\begin{aligned} H_p^6 &= \langle r^6 \rangle_p, \quad H_{4p} = 7r_p^2 \langle r^4 \rangle_p, \quad H_{2p} = \frac{35}{2}r_p^4 \langle r^2 \rangle_p, \\ H_{W_p} &= \langle r^6 \rangle_{W_p} + 7 \left(r_p^2 + \frac{3}{2M^2} \right) \langle r^4 \rangle_{W_p} + \frac{35}{2} \left(r_p^4 + \frac{2r_p^2}{M^2} + \frac{3}{M^4} \right) \langle r^2 \rangle_{W_p}, \\ H_{4n} &= -7(r_+^2 - r_-^2) \langle r^4 \rangle_n \frac{N}{Z}, \quad H_{2n} = -\frac{35}{2}(r_+^4 - r_-^4) \langle r^2 \rangle_n \frac{N}{Z}, \\ H_{W_n} &= - \left[\langle r^6 \rangle_{W_n} + 7 \left(s_2 + \frac{3}{2M^2} \right) \langle r^4 \rangle_{W_n} + \frac{35}{2} \left(s_4 + \frac{2}{M^2}s_2 + \frac{3}{M^4} \right) \langle r^2 \rangle_{W_n} \right] \frac{N}{Z}. \end{aligned}$$

with

$$Q_\tau^4 = \langle r^4 \rangle_\tau, \quad R_\tau^2 = \langle r^2 \rangle_\tau. \quad (13)$$

The notation $\langle r^n \rangle_{W_\tau}$ is defined as

$$\langle r^n \rangle_{W_\tau} = \frac{1}{N_\tau} \int d^3r r^n W_\tau(r),$$

where N_τ represents Z and N for $\tau = p$ and $\tau = n$, respectively.

The non-relativistic expression of the sixth moment which is equivalent to the above relativistic one up to $1/M^2$ may be obtained by the Foldy-Wouthuysen(F-W) transformation[5]. For the phenomenological non-relativistic models, however, it is not possible to derive the consistent relativistic corrections to them, since their original four-component frameworks are not known. In the present paper, the free Dirac equation is employed as the nuclear part of the relativistic Hamiltonian for the F-W transformation[5, 6]. Then, the non-relativistic expression of the sixth moment is obtained from Eq.(10) by replacing the relativistic matrix elements $\langle r^n \rangle_\tau$ and $\langle r^n \rangle_{W_\tau}$ with $\langle r^n \rangle_{nr+r,\tau}$ and $\langle r^n \rangle_{nr,W_\tau}$, respectively,

$$\langle r^n \rangle_{nr+r,\tau} = \langle r^n \rangle_{nr,\tau} + \frac{n(n+1)}{8M^2} \langle r^{n-2} \rangle_{nr,\tau} + \frac{1}{2\mu_\tau} \langle r^n \rangle_{nr,W_\tau}, \quad (14)$$

$$\langle r^n \rangle_{nr,W_\tau} = \frac{n}{N_\tau} \frac{\mu_\tau}{2M^2} \langle 0 | \sum_{k \in \tau} r_k^{n-2} \ell_k \cdot \sigma_k | 0 \rangle_{nr}, \quad (15)$$

where the subscript nr of the matrix elements in the right-hand sides indicates that they should be calculated in the two-component framework of the wave functions⁴.

3 Components of the sixth moment of the charge density

Before the LSA is performed in the next section, it will be shown in this section how each component in Eq.(11) and (12) contributes to H_c^6 by taking a few MF-models. Table 1 and

⁴The last term in the parenthesis of Eq.(28) in Ref.[6] is missed in the relativistic correction of Ref.[5].

	H_c^6	H_{cp}^6	H_p^6	H_{4p}	H_{2p}	H_{W_p}
NL3						
^{40}Ca	4817.801	5001.186	3878.987	990.211	118.059	8.620
^{48}Ca	4100.526	4588.453	3485.765	958.790	118.189	20.400
^{208}Pb	52219.819	55001.458	48112.714	6006.507	308.614	568.314
NL-SH						
^{40}Ca	4616.612	4797.328	3703.400	961.631	116.690	10.299
^{48}Ca	3971.062	4447.191	3362.497	940.040	117.417	21.929
^{208}Pb	50819.698	53558.038	46757.840	5915.257	306.920	572.712
SLy4						
^{40}Ca	5227.890	5405.694	4228.162	1055.877	121.964	-5.617
^{48}Ca	4817.510	5270.163	4075.773	1066.215	124.215	-1.350
^{208}Pb	54008.716	56323.109	49573.044	6098.248	309.751	336.756

Table 1: The sixth moment of the nuclear charge distribution(H_c^6) in ^{40}Ca , ^{48}Ca and ^{208}Pb in units of fm^6 . They are calculated by using parameters of the relativistic nuclear models, NL3[9] and NL-SH[11], and of the non-relativistic one, SLy4[12]. The values of H_{cp}^6 show the contributions from the proton charge distribution to H_c^6 , and other numbers the values of the components of H_{cp}^6 . The neutron charge distribution(H_{cn}^6), which contributes to H_c^6 as $H_c^6 = H_{cp}^6 - H_{cn}^6$, are listed in Table 2. For the details, see the text.

	H_{cn}^6	H_{4n}	H_{2n}	H_{W_n}
NL3				
^{40}Ca	183.385	139.496	30.987	10.969
^{48}Ca	487.927	264.221	50.887	170.114
^{208}Pb	2781.639	1742.852	141.626	894.194
NL-SH				
^{40}Ca	180.717	135.540	30.643	12.602
^{48}Ca	476.129	255.798	50.274	167.352
^{208}Pb	2738.340	1701.125	140.167	894.081
SLy4				
^{40}Ca	177.805	148.495	31.941	-4.562
^{48}Ca	452.653	267.827	51.189	130.933
^{208}Pb	2314.393	1611.226	136.008	564.191

Table 2: The sixth moment of the neutron charge distribution(H_{cn}^6) in ^{40}Ca , ^{48}Ca and ^{208}Pb in units of fm^6 . The values are calculated by using parameters of the relativistic nuclear models, NL3[9] and NL-SH[11], and of the non-relativistic one, SLy4[12]. The others show the values of the components of H_{cn}^6 . For the details, see the text.

H_c^6	FB	SOG	NL3	NL-SH	SLy4
^{40}Ca	$4.234 \times 10^3[4.022]$	$5.390 \times 10^3[4.187]$	4.818×10^3	4.617×10^3	5.228×10^3
^{48}Ca	$3.913 \times 10^3[3.970]$	$4.299 \times 10^3[4.032]$	4.101×10^3	3.971×10^3	4.818×10^3
^{208}Pb	$5.295 \times 10^4[6.128]$	$5.294 \times 10^4[6.128]$	5.222×10^4	5.082×10^4	5.401×10^4

Table 3: The values of the sixth moments(H_c^6) of the charge distributions in ^{40}Ca , ^{48}Ca and ^{208}Pb in units of fm^6 . FB and SOG indicate the Fourier-Bessel- and the sum-of-Gaussian-analyses of the experimental data from electron scattering[4], respectively. In the brackets, the values of H_c are listed in units of fm. The values calculated with the MF-models are given by $H_c^6 = H_{cp}^6 - H_{cn}^6$, where H_{cp}^6 and H_{cn}^6 stand for the sixth moments of the proton and neutron charge distributions, respectively, as listed in Table 1 and 2. NL3[9] and NL-SH[11] are the relativistic MF-models, while SLy4[12] the non-relativistic one. For the details, see the text.

		R_p	R_n	δR	Q_p	Q_{cp}	Q_{cn}
^{40}Ca	RMF	3.348(0.003)	3.297(0.006)	-0.050(0.009)	3.635(0.015)	3.785(0.014)	1.512(0.004)
	SMF	3.348(0.009)	3.304(0.011)	-0.044(0.020)	3.628(0.015)	3.782(0.014)	1.465(0.004)
	Exp.	$R_c = 3.450(0.010)$			$Q_c = 3.761(0.014)$		
^{48}Ca	RMF	3.378(0.005)	3.597(0.021)	0.220(0.026)	3.643(0.014)	3.796(0.012)	1.897(0.006)
	SMF	3.372(0.009)	3.492(0.028)	0.121(0.036)	3.629(0.014)	3.786(0.013)	1.811(0.009)
	Exp.	$R_c = 3.451(0.009)$			$Q_c = 3.736(0.012)$		
^{208}Pb	RMF	5.454(0.013)	5.728(0.057)	0.275(0.070)	5.783(0.023)	5.892(0.022)	2.395(0.008)
	SMF	5.447(0.014)	5.609(0.054)	0.162(0.068)	5.774(0.023)	5.885(0.022)	2.283(0.009)
	Exp.	$R_c = 5.503(0.014)$			$Q_c = 5.851(0.022)$		

Table 4: The results of the least squares analysis taken from Ref.[6]. The numbers in the parentheses for the RMF- and SMF-models denote the error taking account of the experimental one and the standard deviation of the calculated values from the least-squares line. All the numbers are given in units of fm.

2 show the values of the components of H_{cp}^6 and H_{cn}^6 , respectively. They are calculated using the two RMF-models, NL3[9] and NL-SH[11], and the one SMF-model, SLy4[12]. For the SMF models, Eq.(14) and (15) are employed in Eq.(11) and (12). These phenomenological models are constructed so as to reproduce the fundamental quantities of various nuclei like the binding energies, the root msr of the charge distribution, etc., and have widely been used for studying other various nuclear phenomena[8, 14]. The values of the last terms of Eq.(11) and (12) which are not listed in the tables are given, respectively, by

$$\frac{35}{3}r_p^6 = 5.308, \quad \frac{35}{3}(r_+^6 - r_-^6)\frac{N}{Z} = -1.931(^{40}\text{Ca}), -2.704(^{48}\text{Ca}), -2.968(^{208}\text{Pb}).$$

Table 3 compares the MF-results with the experimental values of $H_c^6 = H_{cp}^6 - H_{cn}^6$ which are evaluated by two ways. As mentioned in the previous section, the one is calculated by using the FB-coefficients(FB), and the other the SOG-parameters(SOG) in Ref.[4]. Unfortunately, their experimental errors can not be estimated from the published data[4], where there are not enough information on the experimental and model-dependent errors. Hence, the only four digits as the significant figures are kept, so that the sixth root of H_c^6 in units of fm yields up to the three digits after the decimal point, as in the brackets of Table 3. The numbers listed in Ref.[4] for the root msrs of the charge distributions are given in the same way. The calculated values in Table 1 and 2, however, are shown up to the three digits after the decimal point so as to compare the model-predictions with one another in detail.

Let us go into more details of Table 1, 2 and 3 in order. In Table 1 shows that the main component, H_p^6 , contributes to H_{cp}^6 by more than 75%. The second largest component is H_{4p} , and the sum of H_p^6 and H_{4p} overestimates the FB experimental values of H_c^6 , except for the case of ^{208}Pb by NL-SH. All the calculated values of H_{cp}^6 of ^{48}Ca and ^{208}Pb overestimate the FB and SOG experimental ones. Thus, the negative contributions from the neutron charge density to H_c^6 are definitely required, so as to reproduce the experimental values given by $H_c^6 = H_{cp}^6 - H_{cn}^6$. It is noted that the difference between the values of H_{W_p} in the relativistic and non-relativistic models is not only on their absolute values, but also on their signs in ^{40}Ca and ^{48}Ca , as seen in Table 1.

Tables 1 and 2 show that H_{cn}^6 contributes to H_c^6 by 9 ~ 12% in ^{48}Ca , and by 4 ~ 5% in ^{208}Pb . The neutron contribution is more remarkable in ^{48}Ca , rather than in ^{208}Pb . Almost a

half of the value of H_{4p} is cancelled by H_{cn}^6 in both nuclei. The term, H_{4n} , accounts for more than 50% of H_{cn}^6 . The contribution of H_{2n} depending on R_n^2 is about 10% of H_{cn}^6 in ^{48}Ca , and 5% in ^{208}Pb . In ^{208}Pb , the value of H_{cn}^6 in SLy4 is smaller by more than 15%, compared to that in the RMF.

Table 3 shows that most of the calculated values of H_c^6 are between the FB- and SOG-values. Exceptions are those of SLy4 for ^{48}Ca and ^{208}Pb which overestimate the both FB- and SOG-experimental values. The difference between those of the SLy4 and RMF models stems mainly from their values of H_p^6 , as seen in Table 1. It is noticeable in Table 3 that the experimental value of H_c^6 in ^{40}Ca is larger than that of ^{48}Ca . This fact is reproduced by the three MF models in Table 3. The reason why the value of H_c^6 in ^{40}Ca is larger than that in ^{48}Ca will be discussed in the next section.

For later discussions, the previous results obtained by the LSA in Ref.[6]⁵ are summarized in Table 4. The notation, δR , stands for the neutron-skin thickness, $\delta R = R_n - R_p$, and Q_{cp} and Q_{cn} represent the fourth root of the mean fourth moments of the proton and neutron charge distributions, respectively. The experimental values of R_c and Q_c obtained by FB-method[10] are also listed in Table 4.

The relationship between Q_c , Q_{cp} and Q_{cn} is given by[6],

$$\langle r^4 \rangle_c = Q_c^4 = Q_{cp}^4 - Q_{cn}^4, \quad (16)$$

where Q_{cp}^4 and Q_{cn}^4 are expressed as

$$\begin{aligned} Q_{cp}^4 &= Q_p^4 + Q_{2p} + Q_{2W_p} + Q_{4W_p} + (Q_4)_p, \\ Q_{cn}^4 &= Q_{2n} + Q_{2W_n} + Q_{4W_n} + (Q_4)_n, \end{aligned}$$

with the notations for the protons,

$$Q_{2p} = \frac{10}{3} r_p^2 \langle r^2 \rangle_p, \quad Q_{2W_p} = \frac{10}{3} (r_p^2 + \frac{3}{2M^2}) \langle r^2 \rangle_{W_p}, \quad Q_{4W_p} = \langle r^4 \rangle_{W_p}, \quad (Q_4)_p = \frac{5}{2} r_p^4,$$

and for the neutrons,

$$\begin{aligned} Q_{2n} &= -\frac{10}{3} (r_+^2 - r_-^2) \langle r^2 \rangle_n \frac{N}{Z}, \quad Q_{2W_n} = -\frac{10}{3} (r_p^2 + \frac{3}{2M^2} - \frac{r_+^2 - r_-^2}{\mu_n}) \langle r^2 \rangle_{W_n} \frac{N}{Z}, \\ Q_{4W_n} &= -\langle r^4 \rangle_{W_n} \frac{N}{Z}, \quad (Q_4)_n = -\frac{5}{2} (r_+^4 - r_-^4) \frac{N}{Z}. \end{aligned}$$

Comparing Table 4 to Tables 1 and 2, it is seen that the neutron contribution from H_{cn}^6 to H_c^6 is increased, compared to that from Q_{cn}^4 to Q_c^4 , as expected. Ref.[6] has shown that Q_{2n} is the main component of Q_{cn}^4 , while in H_{cn}^6 , H_{W_n} is much larger than H_{2n} in ^{48}Ca and ^{208}Pb . The contribution from the spin-orbit density is more important in H_{cn}^6 than in Q_{cn}^4 . Increase of the contribution in the relativistic models, compared with that of the non-relativistic models, is due to the fact that the spin-orbit density is enhanced by the small effective mass of nucleon in the relativistic equation of motion[13].

In contrast to the values of H_{cp}^6 of ^{40}Ca and ^{48}Ca in Table 1, those of Q_{cp}^4 in Table 4 are almost the same in the RMF- and SMF-models. Thus, the difference between the models depends on which moment is discussed.

⁵In the column of ^{48}Ca for NL-SH in Table 2 of Ref.[6], the value of 0.780 for Q_{4W_p} is missed. The last three numbers in the column are for Q_{4W_n} , Q_c^4 and Exp., respectively.

4 The least-squares analysis

In the present section, the values of the various moments of the point proton and neutron distributions allowed in the MF-framework are estimated in ^{40}Ca , ^{48}Ca and ^{208}Pb , by the LSA using the experimental values of H_c^6 with the SOG- and FB-methods. The only SOG-values, however, will be indicated in all the figures below, in order to make them simpler. The results using the FB-values will be mentioned, if necessary.

The way of the LSA is the same as that in Ref.[6] for Q_c^4 . First, the values of H_{cp}^6 and H_c^6 calculated in various MF models are plotted in the $(H_{cp}^6 - H_c^6)$ -plane, and the LSL between H_{cp}^6 and H_c^6 is obtained. The value of H_{cp}^6 is determined by the cross point of the LSL and the line of the experimental value of H_c^6 . The determined value is called the LSL-value, as mentioned in §1. Since the LSL-value of H_{cp}^6 is obtained with small standard deviation(σ) and the correlation coefficient(r) nearly equal to 1, it will be used as the ‘quasi-experimental value’ of H_{cp}^6 for other LSA in the following steps. Second, the values of H_p^6 and H_{cp}^6 calculated using the same MF models are plotted in the $(H_p^6 - H_{cp}^6)$ -plane to obtain the LSL for them. The LSL-value of H_p^6 is determined by the cross point of the LSL and the line of the quasi-experimental value of H_{cp}^6 determined in the first step. Third, the values of Q_p^4 are calculated, and are plotted with the calculated values of H_{cp}^6 in the $(Q_p^4 - H_{cp}^6)$ -plane. The cross point of the LSL for $(Q_p^4 - H_{cp}^6)$ and the line of the quasi-experimental value of H_{cp}^6 give the value of Q_p^4 in the MF-framework. Fourth, the same procedure is repeated in order to estimate the values of R_p^2 . Fifth, the values of Q_n^4 and H_{cn}^6 are calculated and are plotted in the $(Q_n^4 - H_{cn}^6)$ -plane to obtain their LSL. In order to obtain the quasi-experimental value of H_{cn}^6 , Eq.(10) is employed with the quasi-experimental one of H_{cp}^6 . The value of Q_n^4 is determined by the cross point of the LSL between Q_n^4 and H_{cn}^6 and the line of the quasi-experimental value of H_{cn}^6 . Finally, the values of R_n^2 are calculated, and are plotted with H_{cn}^6 . The value of R_n^2 in the used model-framework is determined by the cross point of the LSL between R_n^2 and H_{cn}^6 and the line of the quasi-experimental value of H_{cn}^6 .

In Ref.[6] the LSL-values of R_n^2 , R_p^2 , and Q_p^4 have been estimated for ^{40}Ca , ^{48}Ca and ^{208}Pb , by using the experimental values of R_c^2 and Q_c^4 obtained from the FB-analysis in Refs.[4, 10]. In the present paper, the LSL-values of H_p^6 and Q_n^4 will be also determined by using the experimental values of H_c^6 from the both FG- and SOB-analyses.

In the following subsections, the sixth moments of the charge density in ^{40}Ca , ^{48}Ca and ^{208}Pb will be analyzed. The MF-models employed in the present paper are the same as those in Ref.[6]. They are 11 kinds of parameterization for nuclear interactions as RMF-models and 9 kinds of parameterization as the SMF-models, which are chosen arbitrarily among more than 100 models accumulated in nuclear physics[8, 14]. We number them, following Ref.[6] as, 1 L2[15], 2 NLB[15], 3 NLC[15], 4 NL1[16], 5 NL3[9], 6 NL-SH[11], 7 NL-Z[17], 8 NL-S[18], 9 NL3II[19], 10 TM1[20] and 11 FSU[21] for relativistic models, and 1 SKI[22], 2 SKII[22], 3 SKIII[23], 4 SKIV[23], 5 SkM*[24], 6 SLy4[12], 7 T6[25], 8 SGII[26], and 9 Ska[27] for non-relativistic models. The above numbering will be used throughout the present paper.

4.1 ^{40}Ca

Figure 2 shows the relationship between H_{cp}^6 and H_c^6 in ^{40}Ca . The calculated values with the RMF-models are indicated by the closed circles, while those with the SMF-ones are by the open circles. Each circle in the figure bears the number to specify the corresponding nuclear model mentioned in the above. The LSLs are shown for the RMF- and SMF-models, separately,

because there is no reason why they should be taken into account together[6, 28]. The equations of the LSLs and their standard deviations(σ) are listed in the last of the subsection as Table 5. Both RMF- and SMF-models provide almost the same LSLs with the small values of σ as 0.7718 and 1.5701, respectively, and with the correlation coefficient to be about 1.0000. The two LSLs cross the horizontal line which expresses the SOG experimental value of H_c^6 indicated on the right-hand side of the figure. The values of the intersection points are described on the top of the figure for the RMF(rel.)- and SMF(non.)-frameworks, respectively. Those are the LSL-values of H_{cp}^6 accepted in the RMF- and SMF-ones, according to the LSA. They are 5581.031 and 5572.169 fm⁶ in the RMF- and SMF-frameworks, respectively, which will be used below as a ‘quasi-experimental value’ in ⁴⁰Ca. The way of the designation in Fig. 2 will be used in all the following figures in the present paper.

It is seen in Fig. 2 that the RMF- and SMF-models underestimate the experimental value of H_c^6 . As a result, the LSL-value of H_{cp}^6 allowed by the MF-frameworks is much larger than the values calculated with the MF-models used in the present LSA. For latter discussions in §5, the experimental value of H_c^6 obtained from the FB-analysis in Table 3 should be remembered. The FB-value is 4.234×10^3 fm⁶, which is overestimated by all the MF-models except for SKI(1) in Fig. 2, in contrast to the SOG-value given by 5.390×10^3 fm⁶.

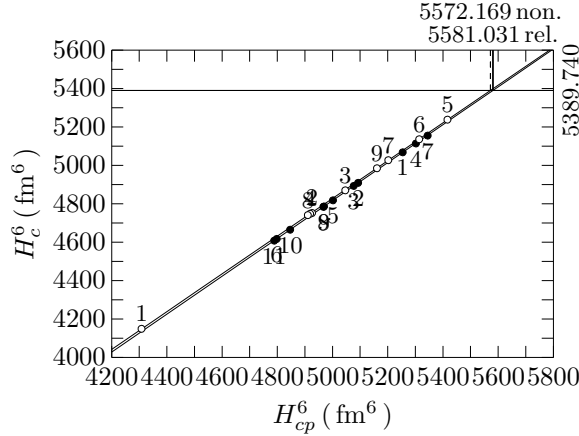


Figure 2: The sixth moment of the charge density(H_c^6) as a function of the sixth moment of the proton charge density(H_{cp}^6) in ⁴⁰Ca. The closed(open) circles are calculated in various relativistic(non-relativistic) mean-field models. The number assigned to each circle represents a model used in the calculations as explained in the text. The lines of the least-square fitting are shown by the solid ones for the relativistic and non-relativistic models, respectively. Those lines cross the horizontal line which expresses the experimental value indicated on the right-hand side of the figure. Their intersection points are described on the top of the figure for the relativistic(rel.) and non-relativistic(non.) frameworks, respectively. The values of the slope(a), the intercept(b) and the standard deviation(σ) of the least-squares lines are listed in Table 5 in the last of the present subsection. For details, see the text.

In Fig. 3 is shown H_{cp}^6 as a function of H_p^6 . Here, the LSL-values of H_{cp}^6 determined in Fig. 2 are used as the quasi-experimental value, as shown by the solid and dashed horizontal lines for the RMF- and SMF-models, respectively. The calculated values in the RMF- and SMF-models distribute over the similar region of the LSLs with the correlation coefficients, $r = 0.9996$ and 0.9998 , respectively, but underestimate the LSL-values of H_p^6 . The order of the MF-models according to the magnitude of H_p^6 is almost the same as that of Fig. 2, and will also be seen to be the same as those of Fig. 4 for Q_p^4 and of Fig. 5 for R_p^2 .

Figure 4 shows H_{cp}^6 as a function of Q_p^4 in ⁴⁰Ca. As in Figs. 2 and 3, both RMF- and

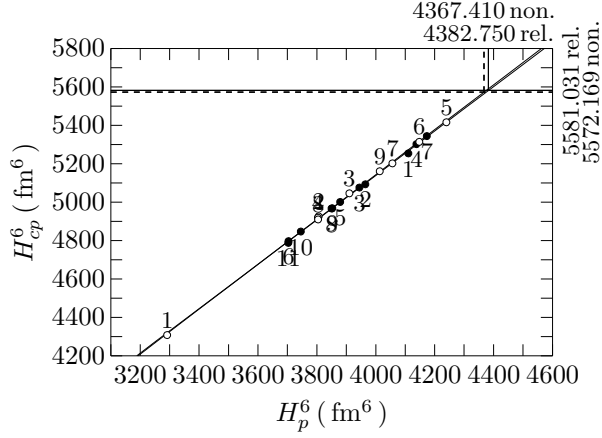


Figure 3: The sixth moment of the proton charge density(H_{cp}^6) as a function of the sixth moment of the point proton distribution(H_p^6) in ^{40}Ca . The solid and dashed horizontal lines indicate the quasi-experimental values of H_{cp}^6 for the RMF- and SKM-models, respectively. The designation in the figure is the same as in Fig.2. For details, see the text.

SMF-models underestimate the LSL-values of Q_p^4 . The standard deviations of the LSLs are a little large, compared with those in Figs 2 and 3, but their correlation coefficients are still close to 1.0000, as $r = 0.9830$ and 0.9945 in RMF- and SMF-frameworks, respectively.

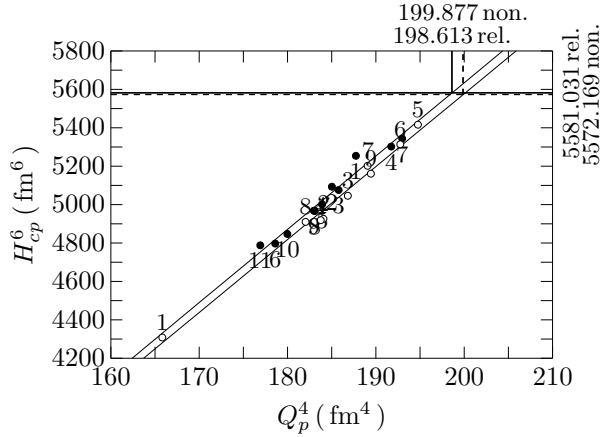


Figure 4: The sixth moment of the proton charge density(H_{cp}^6) as a function of the fourth moment of the point proton distribution(Q_p^4) in ^{40}Ca . The designation in the figure is the same as in Fig.2. For details, see the text.

Figure 5 shows the correlation of R_p^2 with H_{cp}^6 . As seen in Table 1, H_{2p} with R_p^2 contributes to H_{cp}^6 by only about 2%, but they are well correlated with $r = 0.9466$ and 0.9729 in the RMF- and SMF-models, respectively. The LSL-values of R_p^2 determined from H_{cp}^6 in Fig. 5 will be compared to those from R_c^2 and Q_c^4 in Ref.[6] in §5.

Figure 6 shows the correlation between Q_n^4 and H_{cn}^6 . They are related as in Eq.(12), where Q_n^4 is defined as $\langle r^4 \rangle_n$ in H_{4n} . As mentioned before, the quasi-experimental values of H_{cn}^6 are obtained from the experimental value of H_c^6 and the LSL-values of H_{cp}^6 by using the definition in Eq.(10). The differences between the quasi-experimental values of H_{cn}^6 and between the LSLs in the two frameworks in Fig. 6 are understood in the same way as in Figs. 8 and 9 of Ref.[6] for the $(R_n^2 - Q_{cn}^4)$ -correlation. Fig. 8 in Ref.[6] shows similar differences to those in Fig. 6, while such differences disappear in neglecting artificially the spin-orbit densities in the both frameworks, as exhibited in Fig. 9 in Ref.[6].

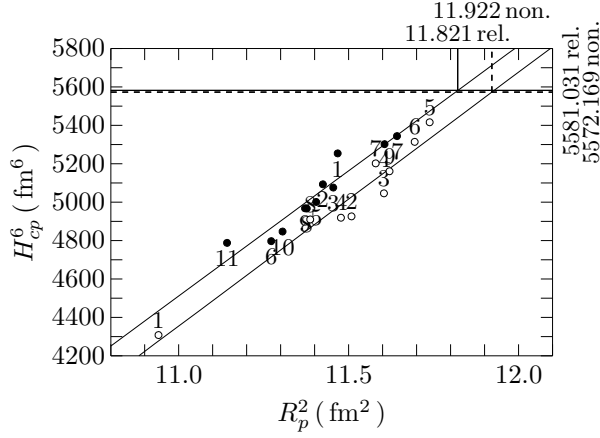


Figure 5: The sixth moment of the proton charge density(H_{cp}^6) as a function of the mean square radius of the point proton distribution(R_p^2) in ^{40}Ca . The designation in the figure is the same as in Fig.2. For details, see the text.

The order of the MF-models according to the magnitude of H_{cn}^6 is almost the same as that of H_{cp}^6 in Fig. 2. All the calculated values of Q_n^4 indicated by the circles underestimate their LSL-values obtained as 185.130 and 187.254 fm^4 for the RMF- and SMF-scheme, respectively.

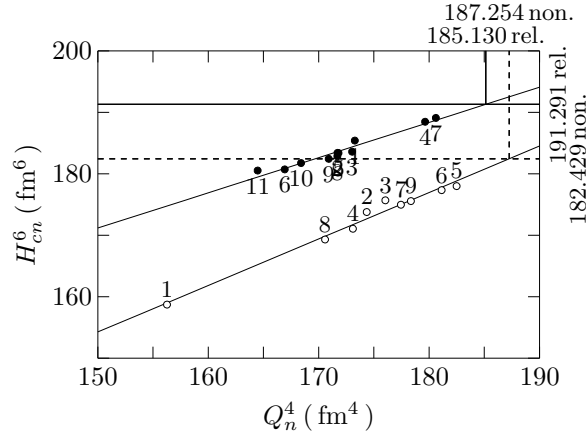


Figure 6: The sixth moment of the neutron charge density(H_{cn}^6) as a function of the fourth moment of the point neutron distribution(Q_n^4) in ^{40}Ca . The designation in the figure is the same as in Fig.2. For details, see the text.

Figure 7 shows the correlation of H_{cn}^6 with R_n^2 . The LSL-values are underestimated by the calculated values in the same way as in the previous figures. The value of the correlation coefficient of the relativistic models in this figure is the worst among those in ^{40}Ca , but is $r = 0.9393$, while that of the non-relativistic models 0.9978.

The distribution of the circles in Fig. 7 is similar to that in Fig. 6. The difference between the LSLs is understood in the same way as in the previous figure, as a result of the different contributions from the spin-orbit densities in the two frameworks. The spin-orbit densities make the difference between the two LSLs clear, but change a little the LSL-values of R_n^2 [6].

Comparing Fig. 5 to Fig. 7, the LSL-value of R_p^2 is larger than that of R_n^2 in both the RMF- and SMF-models. In the same way, the LSL-value of Q_p^4 in Fig. 4 is larger than that of Q_n^4 in Fig. 6. This result will be discussed in the following section, together with those in ^{48}Ca and ^{208}Pb .

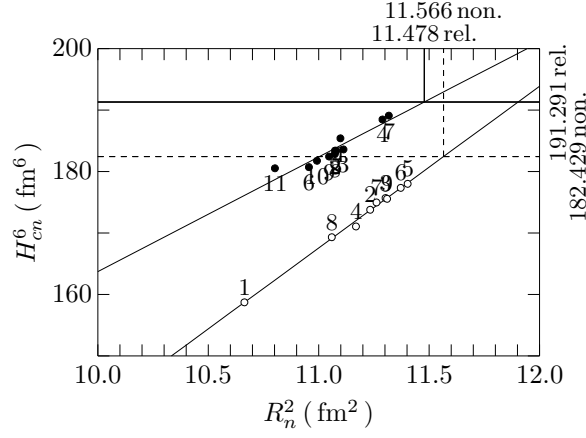


Figure 7: The sixth moment of the neutron charge density(H_{cn}^6) as a function of the mean square radius of the point neutron distribution(R_n^2) in ^{40}Ca . The designation in the figure is the same as in Fig.2. The values of the slope(a), the intercept(b) and the standard deviation(σ) of the LSL are listed in Table 5. For details, see the text.

^{40}Ca			RMF			SMF		
Fig.	y	x	a	b	σ	a	b	σ
2	H_c^6	H_{cp}^6	0.9861	-113.9240	0.7718	0.9823	-84.0148	1.5701
3	H_{cp}^6	H_p^6	1.1562	513.4843	5.2550	1.1681	470.4801	6.3564
4	H_{cp}^6	Q_p^4	38.1642	-1998.8749	34.2842	37.9642	-2016.0047	31.9634
5	H_{cp}^6	R_p^2	1302.8780	-9820.5972	60.1324	1321.1766	-10178.3905	70.5973
6	H_{cn}^4	Q_n^4	0.5730	85.2020	0.6011	0.7563	40.8045	0.8066
7	H_{cn}^6	R_n^2	18.6692	-22.9990	0.9256	26.3194	-121.9817	0.3715

Table 5: The least-squares line $y(x) = ax + b$ and the standard deviation σ depicted in Figure 2 to 7 for the relativistic(RMF) and the non-relativistic(SMF) models.

4.2 ^{48}Ca

Figure 8 shows the relationship between H_{cp}^6 and H_c^6 in ^{48}Ca . The correlation coefficients are 0.9987 and 0.9992 for the RMF- and SMF-models, respectively, and the equations of LSLs are listed, together with their standard deviations, in Table 6 at the end of this subsection.

The LSL-values of H_{cp}^6 accepted in the RMF- and SMF-models are 4805.335 and 4721.394 fm⁶ in the RMF- and SMF-schemes, respectively. In contrast to the case of ^{40}Ca , the calculated values of H_c^6 and H_{cp}^6 in the RMF-models other than NL-Z(7) underestimate the ones of their experimental and LSL-values, while those of the SMF-models, except for SKI(1), overestimate them. The mean values of H_c^6 and H_{cp}^6 in the RMF models are smaller than those in the SMF ones, whereas the LSL-value of H_{cp}^6 in the RMF-framework is larger than that in the SMF-one.

The experimental value, 4298.520 fm⁶, of H_c^6 in ^{48}Ca is smaller than that, 5389.740 fm⁶, in ^{40}Ca . Its main reason is due to the increasing negative contribution from the neutron charge density. Moreover, it should be noticed that the LSL-values of H_{cp}^6 are also smaller in ^{48}Ca than those in ^{40}Ca in Fig. 2. These results will be understood from Fig. 9, which shows that the LSL-values of H_p^6 is smaller in ^{48}Ca than those in ^{40}Ca in Fig. 3.

In Fig. 9 is shown H_{cp}^6 as a function of H_p^6 in ^{48}Ca . The calculated values of the RMF- and SMF-models are almost on the same line, but most of the former underestimate the LSL-value,

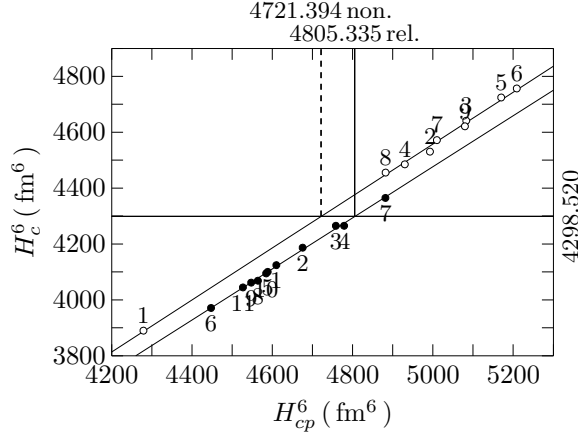


Figure 8: The sixth moment of the charge density(H_c^6) as a function of the sixth moment of the proton charge density(H_{cp}^6) in ^{48}Ca . The designation in the figure is the same as in Fig.2. The values of the slope(a), the intercept(b) and the standard deviation(σ) of the LSLs are listed in Table 6. For details, see the text.

whereas the latter overestimate their LSL-value. As mentioned before, both LSL-values of H_p^6 are smaller than those in ^{40}Ca in Fig. 3. The three examples in Table 1 shows also such a tendency, in contrast to H_{2p} with R_p^2 . Thus, higher moments reveal not only the contribution of the neutron charge density, but also the detailed change of the point proton distributions in the isotopes.

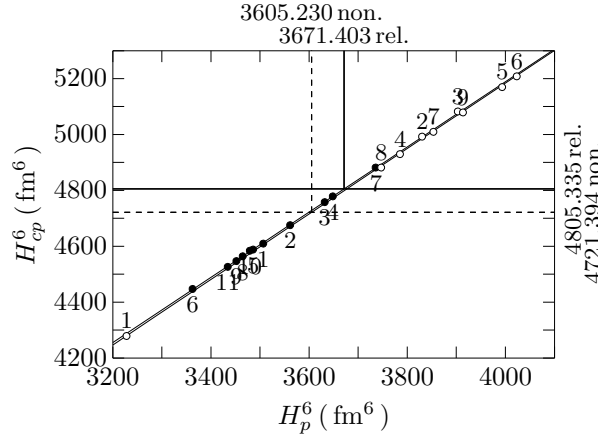


Figure 9: The sixth moment of the proton charge density(H_{cp}^6) as a function of the sixth moment of the point proton distribution(H_p^6) in ^{48}Ca . The designation in the figure is the same as in Fig.2. For details, see the text.

Figure 10 shows the correlation between Q_p^4 and H_{cp}^6 in ^{48}Ca . The RMF-models underestimate again the LSL-value, while the SMF-ones except for SKI(1) overestimate their LSL-value in the same way as in Fig. 9. The LSL-values of Q_p^4 are given as 183.914 and 182.500 fm^4 in the RMF- and SMF-frameworks, respectively. They are smaller than those in ^{40}Ca in Fig. 4 showing 198.613 and 199.877 fm^4 . It should be noted that in contrary to the SOG-value, the FB-one in Table 3 yields the smaller LSL-values in ^{40}Ca as 167.897 and 168.880 fm^4 in the RMF- and SMF-schemes, respectively than 172.420 and 171.436 fm^4 in ^{48}Ca . As for H_p^6 , both the SOG- and FB-values yield the larger LSL-values in ^{40}Ca than those in ^{48}Ca .

Figure 11 shows H_{cp}^6 as a function of R_p^2 in ^{48}Ca . The contribution of R_p^2 through H_{2p} to H_{cp}^6 is small, as seen in Table 1, they are well correlated with the values of r to be 0.9613 and 0.9572

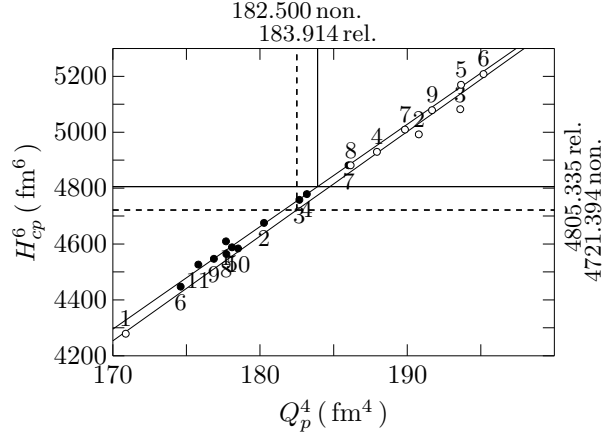


Figure 10: The sixth moment of the proton charge density(H_{cp}^6) as a function of the fourth moment of the point proton distribution(Q_p^4) in ^{48}Ca . The designation in the figure is the same as in Fig.2. For details, see the text.

for RMF- and SMF-models, respectively. The distribution of the circles is almost the same as those for H_{cp}^6 , H_p^6 and Q_p^4 in Figs. 8 to 10.

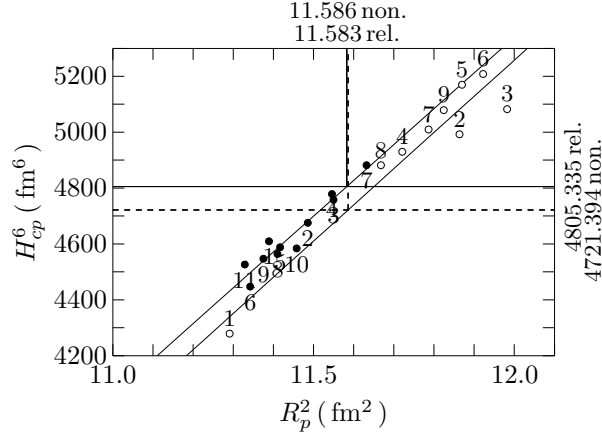


Figure 11: The sixth moment of the proton charge density(H_{cp}^6) as a function of the mean square radius of the point proton distribution(R_p^2) in ^{48}Ca . The designation in the figure is the same as in Fig.2. For details, see the text.

The correlation of Q_n^4 with H_{cn}^6 in ^{48}Ca is shown in Fig. 12. The values of r are obtained as 0.9669 and 0.9902 for the RMF- and SMF-frameworks, respectively. The quasi-experimental values of H_{cn}^6 for the two frameworks are different, since they are obtained by Eq.(10) using the values of H_{cp}^6 given to each framework by Fig. 8. The difference between the two LSLs in Fig. 12 is owing mainly to the different contributions from H_{Wn} to H_{cn}^6 in the RMF- and SMF-models, as seen in Table 2.

On the one hand, in Fig. 10, the calculated values of Q_p^4 in the RMF-models are smaller than the values of the SMF-ones, except for SKI(1), but their LSLs yield the almost same LSL-values of Q_p^4 . On the other hand, in Fig. 12, most of the calculated values of Q_n^4 are distributed over the same region between 220 and 250 fm^4 , but the LSL-values of the RMF- and SMF-frameworks are different from each other, as shown on the top of the figure as 244.1112 and 217.569 fm^4 , respectively. These values together with the LSL-values in Fig. 10 provide $\delta Q = Q_n - Q_p = 0.2701$ and 0.1651 fm in the RMF- and SMF-frameworks, respectively, which show the value of δQ in the RMF-one is larger by about 0.105 fm than that in the SMF-one, in

a similar way as for the neutron skin thickness defined by $\delta R = R_n - R_p$ in Refs.[6, 29].

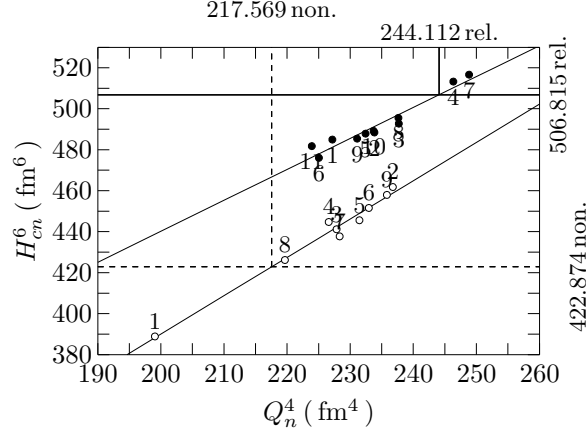


Figure 12: The sixth moment of the neutron charge density(H_{cn}^6) as a function of the fourth moment of the point neutron distribution(Q_n^4) in ^{48}Ca . The designation in the figure is the same as in Fig.2. For details, see the text.

Figure 13 shows the correlation of R_n^2 with H_{cn}^6 in ^{48}Ca . The values of the correlation coefficients are 0.9267 for the RMF-models, while 0.9958 for the SMF-ones. The former value is the worst among those for ^{48}Ca . The distribution of the calculated circles is similar to that in Fig. 12. The line-spacing between the two LSLs is also almost the same as in Fig. 12. Most of the circles by both the RMF- and SMF-models are in the same region of R_n^2 around 13 fm^2 , in contrast to those for the protons in Fig. 11 where all of the closed circles distribute over the lower region of R_p^2 than the open circles, except for that of SKI(1). However, whereas the LSL-values of R_p^2 are almost the same in the RMF- and SMF-schemes in Fig. 11, the LSL-values of R_n^2 are different from each other in Fig. 13. The LSL-value of R_n^2 in the RMF-framework is 13.282 fm^2 which is underestimated by the most of the solid circles, while that in the SHF-one 12.622 fm^2 which is overestimated by the open ones, except for SKI(1). The two LSL-values yield the difference between R_n -values between the RMF- and SMF-schemes to be about 0.092 fm , which is almost equal to 0.105 fm of the difference between δQ mentioned before.

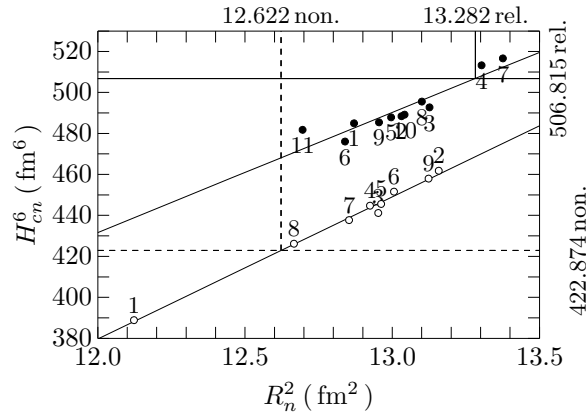


Figure 13: The sixth moment of the neutron charge density(H_{cn}^6) as a function of the mean square radius of the point neutron distribution(R_n^2) in ^{48}Ca . The designation in the figure is the same as in Fig.2. For details, see the text.

^{48}Ca			RMF			SMF		
Fig.	y	x	a	b	σ	a	b	σ
8	H_c^6	H_{cp}^6	0.9143	-94.8689	5.7064	0.9299	-91.8221	9.4474
9	H_{cp}^6	H_p^6	1.1673	519.8788	1.8854	1.1714	498.3485	5.8241
10	H_{cp}^6	Q_p^4	36.6766	-1940.0028	14.8622	37.4618	-2115.3859	26.9812
11	H_{cp}^6	R_p^2	1281.5133	-10038.2548	33.5842	1295.7757	-10291.3620	75.2733
12	H_{cn}^4	Q_n^4	1.5108	138.0005	3.0357	1.8709	15.8312	2.8757
13	H_{cn}^6	R_n^2	58.6328	-271.9630	4.4745	69.3482	-452.4638	1.8884

Table 6: The least-squares line $y(x) = ax + b$ and the standard deviation σ depicted in Figure 8 to 13 for the relativistic(RMF) and the non-relativistic(SMF) models.

4.3 ^{208}Pb

As shown in Ref.[6], the experimental values of R_c^2 and Q_c^4 of ^{208}Pb are well reproduced by both RMF- and SMF-models, unlike those of ^{40}Ca and ^{48}Ca . Fig. 14 shows the correlation between H_{cp}^6 and H_c^6 in ^{208}Pb . The circles of the calculated values are distributed over both the left- and right-hand sides of the LSL-values of H_{cp}^6 . This fact implies that the mean value of H_c^6 , $\langle H_c^6 \rangle$, in the MF-models well reproduce the SOG-value and that the value of $\langle H_{cp}^6 \rangle$ is nearly equal to its LSL-value. The difference between the LSL-values of the RMF- and SMF-models in Fig. 14 is about 1% of their values. For ^{208}Pb , the FB- and SOG-analyses provide almost the same experimental value as shown in Table 3, although Appendix indicates unphysical r -dependences in the charge distributions. In contrast to Fig. 14, Figs. 2 and 8 have shown a disagreement of the values of $\langle H_c^6 \rangle$ in ^{40}Ca and ^{48}Ca with the SOG-values.

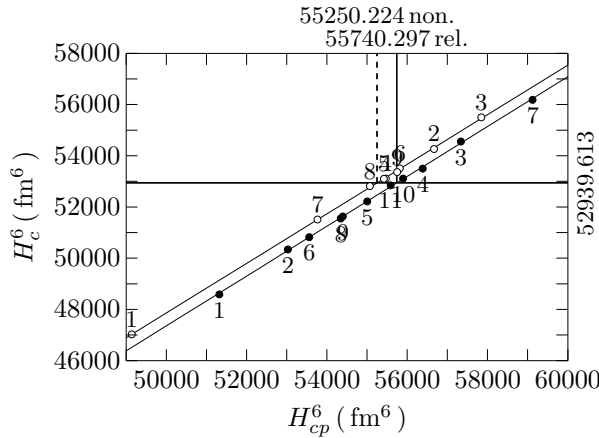


Figure 14: The sixth moment of the charge density(H_c^6) as a function of the sixth moment of the point proton charge density(H_{cp}^6) in ^{208}Pb . The designation in the figure is the same as in Fig.2. The values of the slope(a), the intercept(b) and the standard deviation(σ) of the LSLs are listed in Table 7. For details, see the text.

The correlation of H_{cp}^6 with H_p^6 is depicted in Fig. 15, which shows that most of the circles are near the LSL-values of H_p^6 . The difference between the LSL-values of H_p^6 in the RMF- and SMF-frameworks is less than 1% of their values, as in the previous figure .

Figure 16 shows the correlation between Q_p^4 and H_{cp}^6 . The ratio of the LSL-value of Q_p^4 from H_{cp}^6 to that from Q_{cp}^4 in Ref.[6] is, for example, about 1.007 in the RMF-framework. Such a small difference in ^{208}Pb is owing to the fact that the LSL-values of Q_p^4 are almost reproduced

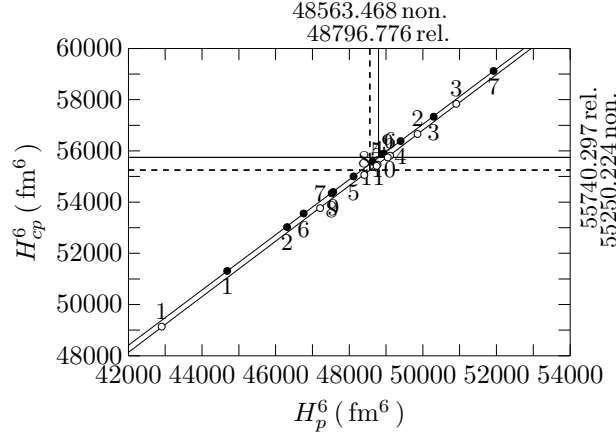


Figure 15: The sixth moment of the proton charge density(H_{cp}^6) as a function of the sixth moment of the point proton distribution(H_p^6) in ^{208}Pb . The designation in the figure is the same as in Fig.2. For details, see the text.

by the mean values calculated with the models in both $(Q_p^4 - Q_{cp}^4)$ - and $(Q_p^4 - H_{cp}^6)$ -correlations for ^{208}Pb , as will be discussed in the next section.

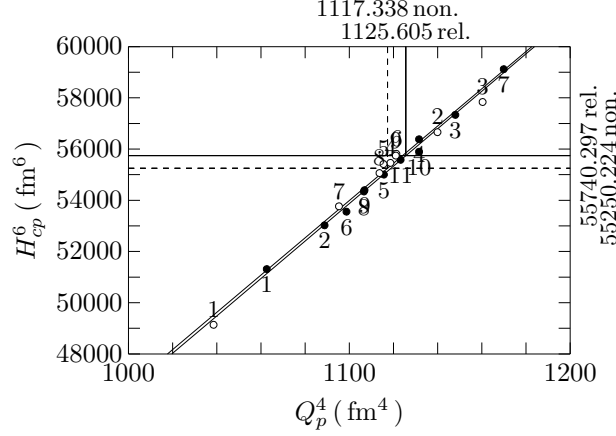


Figure 16: The sixth moment of the proton charge density(H_{cp}^6) as a function of the fourth moment of the point proton distribution(Q_p^4) in ^{208}Pb . The designation in the figure is the same as in Fig.2. For details, see the text.

In Fig. 17 is shown the correlation of R_p^2 with H_{cp}^6 in a similar way as for previous figures. Although the contribution of H_{2p} with R_p^2 to H_{cp}^6 is small as in Table 1, the values of r is obtained as 0.9878 and 0.9559, for the RMF- and SMF-models, respectively. The LSL-value of R_p^2 are 29.935 in the RMF-framework, while 29.810 fm^2 in the SMF-one. Ref.[6] provides 29.843(0.252) and 29.738(0.295) fm^2 obtained from Q_{cp}^4 , and 29.733(0.155) and 29.671(0.154) fm^2 from R_c^2 in the RMF- and SMF-frameworks, respectively. The present values are slightly larger than the previous ones.

Figure 18 shows the correlation between Q_n^4 and H_{cn}^6 . The values of r are obtained as 0.9442 and 0.9982 in the RMF- and SMF-models, respectively. The quasi-experimental value of H_{cn}^6 is obtained by Eq.(10) using the LSL-values of H_{cp}^6 in Fig. 14. Hence, the difference between the quasi-experimental values of H_{cn}^6 is the same as that between the LSL-values of H_{cp}^6 in Fig. 14 for the RMF- and SMF-frameworks. In the RMF-framework, the ratio of the quasi-experimental value of H_{cn}^6 to the experimental one of H_c^6 is 0.053, whereas that of Q_{cn}^4 to Q_c^4 is 0.028 in Ref.[6]. Thus, the neutron contribution is increased in H_c^6 , compared to that in Q_c^4 .

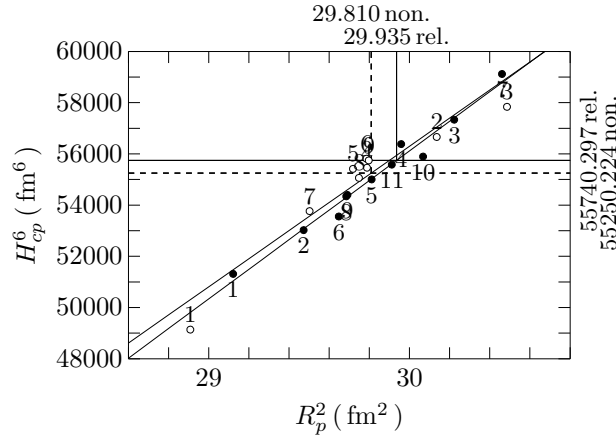


Figure 17: The sixth moment of the proton charge density(H_{cp}^6) as a function of the mean square radius of the point proton distribution(R_p^2) in ^{208}Pb . The designation in the figure is the same as in Fig.2. For details, see the text.

The spacing between the two LSLs comes from the difference between the values of H_{W_n} in the RMF- and SMF-models, as in Table 2. In contrast to the case of ^{48}Ca in Fig. 12, the calculated values of Q_n^4 in the RMF- and SMF-models are distributed over regions near their LSL-values.

On the one hand, Fig. 16 yields almost the same LSL-values of Q_p^4 in the RMF- and SMF-frameworks. The difference between them is less than 1%. On the other hand, those of Q_n^4 in Fig. 18 are different from each other by about 9%. These values provide $\delta Q = Q_n - Q_p = 0.3345$ and 0.2032 fm in the RMF- and SMF-frameworks, respectively, which show the value of δQ in the RMF-one is larger by about 0.131 fm than that in SMF-one, in a similar way as in ^{48}Ca .

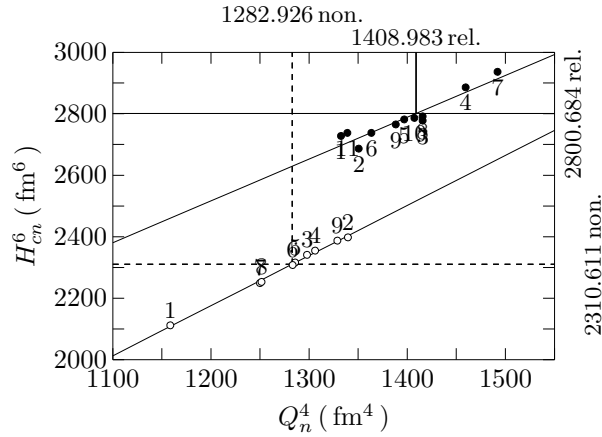


Figure 18: The sixth moment of the neutron charge density(H_{cn}^6) as a function of the fourth moment of the neutron distribution(Q_n^4) in ^{208}Pb . The designation in the figure is the same as in Fig.2. For details, see the text.

The correlation of R_n^2 with H_{cn}^6 in ^{208}Pb is shown in Fig. 19. It shows that, although the main component of H_{cn}^6 is H_{4n} with Q_n^4 , as seen in Table 2, the circles for R_n^2 in the small component H_{2n} are distributed in a similar way as in Fig. 18. The values of r are 0.9252 and 0.9980 for the RMF- and SMF-models, respectively. The former is the worst value among those in figures for ^{208}Pb , while the best one 1.0000 for the RMF-models in Fig. 15. The LSL-values of R_n^2 are determined to be 33.070 and 31.611 fm 2 for the RMF- and SMF-frameworks, respectively, while they are obtained to be $32.943(2.934)$ and $31.516(0.657)$ fm 2 from Q_{cn}^4 in Ref.[6]. Although the

^{208}Pb			RMF			SMF		
Fig.	y	x	a	b	σ	a	b	σ
14	H_c^6	H_{cp}^6	0.9737	-1331.9422	41.9577	0.9680	-541.2208	37.8249
15	H_{cp}^6	H_p^6	1.0791	3083.5021	15.8481	1.0841	2603.4186	24.8424
16	H_{cp}^6	Q_p^4	73.0718	-26509.6358	142.0972	72.7496	-26035.6492	287.1230
17	H_{cp}^6	R_p^2	5779.9250	-117283.8075	317.7420	5489.9363	-108404.6446	680.4680
18	H_{cn}^4	Q_n^4	1.3612	882.7338	22.4528	1.6307	218.5919	5.0136
19	H_{cn}^6	R_n^2	118.7533	-1126.5053	25.8644	135.3781	-1968.7570	5.2256

Table 7: The least-squares line $y(x) = ax + b$ and the standard deviation σ depicted in Figure 14 to 19 for the relativistic(RMF) and the non-relativistic(SMF) models.

value of Q_{cn}^4 in Ref.[6] are estimated on the basis of the FB-analysis, the values of R_n^2 contain the present results within their errors.

In the previous papers[6, 29], it has been pointed out that whereas the LSL-values of R_p are almost the same in the RMF- and SMF-frameworks, the LSL-values of R_n are larger by about 0.1 fm in the RMF-framework than those in the SMF-one, in both ^{48}Ca and ^{208}Pb . As a result, their δR s differ from each other by about 0.1 fm. In the same way, the present LSA in Fig. 19 provides the LSL-values of R_n to be larger by about 0.128 fm in the RMF-framework than in the SMF-one. Together with the LSL-values of R_p in Fig. 17, the difference between δR s in the two frameworks is obtained as 0.117 fm. This 0.1 fm difference between δR s in the RMF- and SMF-frameworks is understood, according to Refs.[28, 29]. The difference between δQ s in ^{48}Ca and ^{208}Pb mentioned before may be explained in a similar way as for δR s.

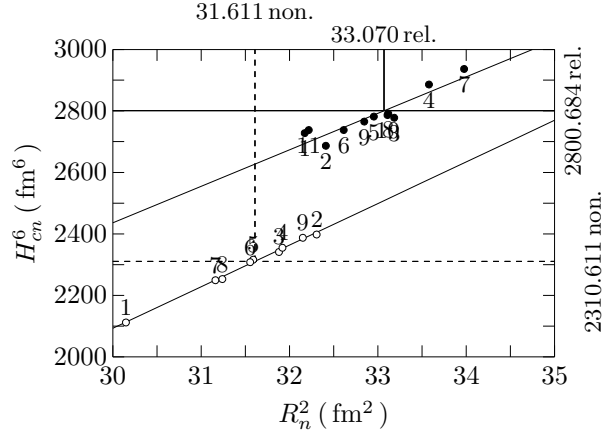


Figure 19: The sixth moment of the neutron charge density(H_{cn}^6) as a function of the mean square radius of the neutron distribution(R_n^2) in ^{208}Pb . The designation in the figure is the same as in Fig.2. For details, see the text.

5 Discussions

The LSA yields for the set of the models the LSLs peculiar to its framework, like the RMF- or the SMF-approximation. The LSLs are expected to be inherent to the framework, and not to depend strongly on the choice of the sample-models for the set. Indeed, there is a following example. The previous authors[30] has explored the correlation between the slope

		$R_{c,\text{exp}}^2 / (\langle R_c^2 \rangle)$	$Q_{c,\text{exp}}^4 / (\langle Q_c^4 \rangle)$	$R_{\tau,\text{LSL}}^2(a_{\tau,2}^{(2)})$	$R_{\tau,\text{LSL}}^2(a_{\tau,2}^{(4)})$	$\langle R_\tau^2 \rangle$
^{48}Ca	RMF	11.910	194.734	p 11.435(1.0195)	11.364(37.0126)	11.448
		/(11.924)	/(197.827)	n	12.839(16.2922)	13.029
	SMF	11.910	194.734	p 11.372(1.0000)	11.336(36.7018)	11.772
		/(12.310)	/(210.706)	n	12.147(22.1955)	12.866
^{208}Pb	RMF	30.283	1171.981	p 29.733(1.0024)	29.843(81.4556)	29.829
		/(30.379)	/(1170.792)	n	32.943(43.1093)	32.929
	SMF	30.283	1171.981	p 29.671(1.0000)	29.738(79.0078)	29.760
		/(30.372)	/(1173.747)	n	31.516(46.2100)	31.545

Table 8: The LSL-values of R_τ^2 in ^{48}Ca and ^{208}Pb listed as $R_{\tau,\text{LSL}}^2(a_{\tau,2}^{(2)})$ and $R_{\tau,\text{LSL}}^2(a_{\tau,2}^{(4)})$. The former is obtained through the experimental values of $R_{c,\text{exp}}^2$, while the latter through the ones of $Q_{c,\text{exp}}^4$. The numbers of $a_{\tau,2}^{(2)}$ and $a_{\tau,2}^{(4)}$ in the parentheses indicate the values of the slopes of the LSL-equations between R_τ^2 and R_c^2 and between R_τ^2 and Q_c^4 , respectively[6]. The mean values of R_c^2 , Q_c^4 and R_τ^2 in the relativistic mean-field (RMF)- and non-relativistic (SMF)-models are expressed as $\langle R_c^2 \rangle$, $\langle Q_c^4 \rangle$ and $\langle R_\tau^2 \rangle$, respectively. The values of R^2 and $a_{\tau,2}^{(4)}$ are given in units of fm^2 , those of Q^4 in units of fm^4 , and the values of $a_{\tau,2}^{(2)}$ have no unit. For details, see the text.

of the asymmetry-energy density(L) and the neutron skin thickness(δR), by the LSA using 47 models in the RMF- and SMF-frameworks. They have analyzed all results in the two framework together, and found the LSL-equation as $\delta R = 0.147 \times 10^{-2}L + 0.101$ with $r = 0.979$. In the present LSA, 11 and 9 models are chosen arbitrarily among the RMF- and SMF-models, respectively[6]. If these 20 models are used in the same purpose as in Ref.[30], one finds the LSL-equation as $\delta R = 0.151 \times 10^{-2}L + 0.102$ with $r = 0.991$ [28], which is almost the same result as that by 47models[30]. Thus, it is reasonable to assume that the LSL does not depend on how the models are chosen for the sample-set in the specified framework.

In the present paper, the moments of the charge distribution have been analyzed. The n th moment($R_c^{(n)}$) is expressed in terms of the $m(\leq n)$ th moments of the point proton distribution($R_p^{(m)}$) and the $m(< (n-2))$ th ones of the point neutron distribution($R_n^{(m)}$) in the nucleus[5]. Then, the LSA is performed between $R_c^{(n)}$ and $R_\tau^{(m)}$ ($\tau = p, n$), whose regression(LSL)-equation is described as

$$R_c^{(n)} = a_{\tau,m}^{(n)} R_\tau^{(m)} + b_\tau^{(n)}, \quad (17)$$

where $a_{\tau,m}^{(n)}$ and $b_\tau^{(n)}$ denote the slope and the intercept of the LSL-equation, respectively. By the definition of LSL, the above equation provides the relationship between the mean values of the moments calculated by the models in the set as,

$$\langle R_c^{(n)} \rangle = a_{\tau,m}^{(n)} \langle R_\tau^{(m)} \rangle + b_\tau^{(n)}. \quad (18)$$

When such equations for the various moments under consideration are solved simultaneously, one obtains the average value of each calculated moment. For example, if one is interested in the five moments, Q_c^4 , Q_{cp}^4 , Q_{cn}^4 , R_p^2 and R_n^2 , then the same number of the LSLs are selected as

$$\begin{aligned} Q_c^4 &= Q_{cp}^4 - Q_{cn}^4, & Q_c^4 &= \alpha_p R_p^2 + \beta_p, & Q_c^4 &= \alpha_n R_n^2 + \beta_n, \\ Q_{cp}^4 &= a_{cp} R_p^2 + b_{cp}, & Q_{cn}^4 &= a_{cn} R_n^2 + b_{cn}. \end{aligned} \quad (19)$$

Employing the LSL-coefficients listed in Table 4 and 5 in Ref.[6], the mean values in ^{48}Ca and ^{208}Pb are obtained as in Table 8.

There is a kind of the sum rule with respect to the coefficients of the LSL-equations. Eqs.(17) and (18) provide

$$R_c^{(n)} - \langle R_c^{(n)} \rangle = a_{\tau,m}^{(n)} \left(R_\tau^{(m)} - \langle R_\tau^{(m)} \rangle \right), \quad (20)$$

which is nothing but the definition of $a_{\tau,m}^{(n)}$ in the $(R_\tau^{(m)}, R_c^{(n)})$ -plane. According to the definition of the moments as in Eqs.(10) and (16), $R_c^{(n)}$ is assumed to be described in the form:

$$R_c^{(n)} = \sum_{\tau,m} \alpha_{\tau,m}^{(n)} R_\tau^{(m)} + \sum_{\tau,m} W_\tau^{(n,m)} + C^{(n)}, \quad (21)$$

where $\alpha_{\tau,m}^{(n)}$ stands for the coefficient coming from the nucleon-size, $W_\tau^{(n,m)}$ the term due to the spin-orbit density, and $C^{(n)}$ term including the nucleon-size only. The examples of $\alpha_{\tau,m}^{(n)}$ and $W_\tau^{(n,m)}$ are given below Eqs.(12) and (16). For example, $\alpha_{p,4}^{(6)} = 7r_p^2$ in H_{4p} of H_{cp}^6 and $W_n^{(4,2)} = Q_{2W_n}$ in Q_{cn}^4 of Q_c^4 . In calculating Eq.(21) by sample-models, the mean values satisfy

$$\langle R_c^{(n)} \rangle = \sum_{\tau,m} \alpha_{\tau,m}^{(n)} \langle R_\tau^{(m)} \rangle + \sum_{\tau,m} \langle W_\tau^{(n,m)} \rangle + C^{(n)}, \quad (22)$$

Eqs.(21) and (22) provide

$$R_c^{(n)} - \langle R_c^{(n)} \rangle = \sum_{\tau,m} \alpha_{\tau,m}^{(n)} \left(R_\tau^{(m)} - \langle R_\tau^{(m)} \rangle \right) + \sum_{\tau,m} \left(W_\tau^{(n,m)} - \langle W_\tau^{(n,m)} \rangle \right). \quad (23)$$

Finally, the above equation and Eq.(20) yield the sum rule on the slopes of the LSL-equations as⁶

$$1 = \sum_{\tau,m} \frac{\alpha_{\tau,m}^{(n)}}{a_{\tau,m}^{(n)}} + \sum_{\tau,m} \frac{1}{a_{W_\tau,m}^{(n)}}. \quad (24)$$

Here, the slope of the LSL-equation with respect to the moment of the spin-orbit density, $a_{W_\tau,m}^{(n)}$, has been defined in the same way as Eq.(17) for the moment, $R_\tau^{(m)}$, as

$$R_c^{(n)} = a_{W_\tau,m}^{(n)} W_\tau^{(n,m)} + b_{W_\tau,m}^{(n)}, \quad (25)$$

which gives a similar equation to Eq.(20) as

$$R_c^{(n)} - \langle R_c^{(n)} \rangle = a_{W_\tau,m}^{(n)} \left(W_\tau^{(n,m)} - \langle W_\tau^{(n,m)} \rangle \right). \quad (26)$$

The study of the LSLs on $W_\tau^{(n,m)}$ is out of the present purpose, but an example is found for ⁴⁸Ca in Fig. 20 of Ref.[6]. It is possible to study the LSL by expanding $W_\tau^{(n,m)}$ in terms of the moments, $\langle r \rangle_{W_\tau}$, of the spin-orbit density as in Eqs.(10) and (16).

When the moment of the charge distribution is written for the protons and the neutrons separately as in Eqs.(10) and (16),

$$R_c^{(n)} = R_{cp}^{(n)} - R_{cn}^{(n)}, \quad (27)$$

and the LSL-equations are obtained as

$$R_{c\tau}^{(n)} = a_{c\tau,m}^{(n)} R_\tau^{(m)} + b_{c\tau}^{(n)}, \quad R_{c\tau}^{(n)} = a_{cW_\tau,m}^{(n)} W_\tau^{(n,m)} + b_{cW_\tau,m}^{(n)}, \quad (28)$$

then the LSL-sum rule is described as

$$1 = \sum_m \frac{\alpha_{\tau,m}^{(n)}}{a_{c\tau,m}^{(n)}} + \sum_m \frac{1}{a_{cW_\tau,m}^{(n)}}. \quad (29)$$

⁶Eq.(24) is derived, assuming Eq.(21). More exact derivation is given in Appendix.

Eq.(24) and (29) are convenient for examining how each moment of the point proton and neutron distributions contributes to the $R_c^{(n)}$, and whether or not the calculations of the LSLs are performed correctly, as for the energy-weighted sum rule in the random phase approximation(RPA)[31, 32, 33, 34].

The LSL-sum rule, Eq.(24), makes clear the relationship between the experimental value of $R_c^{(n)}$ and the LSL-values of the moments. The LSL-value is given by Eq.(17) as

$$R_{c,\text{exp}}^{(n)} = a_{\tau,m}^{(n)} R_{\tau,\text{LSL}}^{(m)}(R_{c,\text{exp}}^{(n)}) + b_{\tau}^{(n)}, \quad (30)$$

where $R_{c,\text{exp}}^{(n)}$ and $R_{\tau,\text{LSL}}^{(m)}(R_{c,\text{exp}}^{(n)})$ stand for the experimental value of $R_c^{(n)}$ and the LSL-value of $R_{\tau}^{(m)}$ determined by $R_{c,\text{exp}}^{(n)}$, respectively. Eqs.(18) and (30) give the relationship between the LSL-value and the mean value as

$$\langle R_{\tau}^{(m)} \rangle = R_{\tau,\text{LSL}}^{(m)}(R_{c,\text{exp}}^{(n)}) + \frac{1}{a_{\tau,m}^{(n)}} \left(\langle R_c^{(n)} \rangle - R_{c,\text{exp}}^{(n)} \right). \quad (31)$$

By inserting the above equation and similar equation of the moment for the spin-orbit density into the right-hand side of Eq.(22), and using the LSL-sum rule, Eq.(24), one obtains

$$R_{c,\text{exp}}^{(n)} = \sum_{\tau,m} \alpha_{\tau,m}^{(n)} R_{\tau,\text{LSL}}^{(m)}(R_{c,\text{exp}}^{(n)}) + \sum_{\tau,m} W_{\tau,\text{LSL}}^{(n,m)}(R_{c,\text{exp}}^{(n)}) + C^{(n)}, \quad (32)$$

where the LSL-value of $W_{\tau}^{(n,m)}$ is defined as $W_{\tau,\text{LSL}}^{(n,m)}(R_{c,\text{exp}}^{(n)})$ in the same way as in Eq.(30) for $R_{\tau}^{(m)}$. Thus, in spite of the fact that the n th moment of the charge density is a function of several moments of the point proton and neutron distributions, the value of each moment is provided uniquely by the LSL-value, $R_{\tau,\text{LSL}}^{(m)}(R_{c,\text{exp}}^{(n)})$, determined through the single experimental value, $R_{c,\text{exp}}^{(n)}$.

It should be noticed that the LSL-values in Eq.(32) depend on n of $R_{c,\text{exp}}^{(n)}$, as explicitly indicated in Eq.(30) as $R_{\tau,\text{LSL}}^{(m)}(R_{c,\text{exp}}^{(n)})$. For example, the value of $R_{p,\text{LSL}}^2(Q_{c,\text{exp}}^4)$ is not necessary to be equal to that of $R_{p,\text{LSL}}^2(R_{c,\text{exp}}^2)$ as

$$R_{p,\text{LSL}}^2(R_{c,\text{exp}}^2) = \langle R_p^2 \rangle - \frac{1}{a_{p,2}^{(2)}} (\langle R_c^2 \rangle - R_{c,\text{exp}}^2), \quad (33)$$

$$R_{p,\text{LSL}}^2(Q_{c,\text{exp}}^4) = \langle R_p^2 \rangle - \frac{1}{a_{p,2}^{(4)}} (\langle Q_c^4 \rangle - Q_{c,\text{exp}}^4). \quad (34)$$

It is natural to expect that there is an ideal set \mathcal{A} of the MF-models, whose mean value $\langle R_c^2 \rangle_{\mathcal{A}}$ reproduces the experimental value of $R_{c,\text{exp}}^2$, because $R_{c,\text{exp}}^2$ is usually used as one of the input-quantities to fix the free interaction parameters. Then, Eq.(33) provides the LSL-value as

$$R_{p,\text{LSL}}^2(R_{c,\text{exp}}^2) = \langle R_p^2 \rangle_{\mathcal{A}}. \quad (35)$$

In order to obtain $R_{p,\text{LSL}}^2(Q_{c,\text{exp}}^4) = R_{p,\text{LSL}}^2(R_{c,\text{exp}}^2)$, Eq.(34) implies that the set \mathcal{A} should reproduce the value of $Q_{c,\text{exp}}^4$ also, as $\langle Q_c^4 \rangle_{\mathcal{A}} = Q_{c,\text{exp}}^4$.

An arbitrary set A in the same framework as for \mathcal{A} does not necessarily satisfy Eq.(35), but is expected to have the same LSL as

$$R_{p,\text{LSL}}^2(R_{c,\text{exp}}^2) = \langle R_p^2 \rangle_A - \frac{1}{a_{p,2}^{(2)}} (\langle R_c^2 \rangle_A - R_{c,\text{exp}}^2). \quad (36)$$

In order for the set A to obtain $R_{p,\text{LSL}}^2(Q_{c,\text{exp}}^4) = R_{p,\text{LSL}}^2(R_{c,\text{exp}}^2)$, Eqs.(33) and (34) require

$$\frac{1}{a_{p,2}^{(4)}} (\langle Q_c^4 \rangle_A - Q_{c,\text{exp}}^4) = \frac{1}{a_{p,2}^{(2)}} (\langle R_c^2 \rangle_A - R_{c,\text{exp}}^2). \quad (37)$$

Similar discussions can be made for other higher moments $R_c^{(n)}$ and their components $R_\tau^{(m)}$.

The MF-framework does not assure that the set \mathcal{A} reproduces the experimental values of the higher moments ($n \geq 4$) by the mean values, and that the set A have the relationship like Eq.(37) for higher moments ($n \geq 4$) also. When the equation like Eq.(37) is not satisfied for $R_c^{(n)}$ ($n \geq 4$), then the MF-framework with $R_{p,\text{LSL}}^2(R_{c,\text{exp}}^2)$ fails to reproduce its experimental value, although Eq.(32) for $R_{c,\text{exp}}^{(n)}$ still holds.

It is explored numerically how the LSL-values of the higher moments are related to that of the lowest moment, $R_{p,\text{LSL}}^2(R_{c,\text{exp}}^2)$, used as an input-quantity. Table 8 lists the values needed for above arguments for Q_c^4 in ^{48}Ca and ^{208}Pb . The mean values of R_c^2 and Q_c^4 are nearly equal to the corresponding experimental values, with one exception. The exception is in the SMF-models for ^{48}Ca which provide 12.310 fm^2 for $\langle R_c^2 \rangle$ against 11.910 fm^2 of the experimental value, and 210.706 fm^4 for $\langle Q_c^4 \rangle$ against 194.734 fm^4 of the experimental one. As a result, apart from the exception, all the models yield each nucleus almost the same values for $R_{p,\text{LSL}}^2(R_{c,\text{exp}}^2)$, $R_{p,\text{LSL}}^2(Q_{c,\text{exp}}^4)$ and $\langle R_p^2 \rangle$, and for $R_{n,\text{LSL}}^2(Q_{c,\text{exp}}^4)$ and $\langle R_n^2 \rangle$. In these calculations, the sample-models seem to play a role of the set \mathcal{A} which reproduces the experimental values of $Q_{c,\text{exp}}^4$ also.

The results of the SMF-models for ^{48}Ca in Table 8 seem to show approximately the relationship in Eq.(37). The values of $R_{p,\text{LSL}}^2(R_{c,\text{exp}}^2)$ and $R_{p,\text{LSL}}^2(Q_{c,\text{exp}}^4)$ are almost the same, as 11.372 and 11.336 fm^2 , while the mean values of $R_p^2 = 11.772 \text{ fm}^2$ are rather different from those LSL-values. Table 8 gives the values of the right-hand side in Eq.(37) to be about 0.435 fm^2 , while that of the left-hand side to be about 0.400 fm^2 . These values compensate the differences between $\langle R_p^2 \rangle$ and $R_{p,\text{LSL}}^2(Q_{c,\text{exp}}^4)$ and between $\langle R_p^2 \rangle$ and $R_{p,\text{LSL}}^2(R_{c,\text{exp}}^2)$, respectively.

Once the experimental values of H_c^6 is determined, then it would be possible to discuss in more detail the n -dependence of the LSL-values, together with the relationship of the LSL-value, $R_{\tau,\text{LSL}}^2(H_{c,\text{exp}}^6)$, to the mean values. Since there are no reliable data on H_c^6 yet, the examples of the predicted values in the present LSA are listed in Table 9. If $R_{p,\text{LSL}}^2(H_{c,\text{exp}}^6)$ is assumed to be equal to $R_{p,\text{LSL}}^2(R_{c,\text{exp}}^2)$, then the values of $H_{c,\text{exp}}^6$ is calculated with Eq.(30) and the coefficients of the LSL-equations, $H_c^6 = aH_{cp}^6 + b$, in Table 5 to 7. Comparing those values with the ones in Table 3, it is seen that the predicted values are fairly different from the FB- and SOG-values. The predicted values for ^{40}Ca and ^{48}Ca are between those by FB- and SOG-method, while the ones for ^{208}Pb are smaller than those of FB- and SOG-analysis. These facts may be expected from Figs. 21, 23 and 25 in Appendix, and affect the LSL-values as in the following Table 10. The last column in Table 9 shows the contribution of the neutrons to the charge distributions. In ^{48}Ca , both the RMF- and SMF-frameworks predict the ratio of H_{cn}^6 to H_{cp}^6 to be about 10%, while Ref.[6] has obtained the value of Q_{cn}^4/Q_{cp}^4 to be about 5%.

Table 10 summarizes the LSL-values of R_p , R_n and Q_p determined by the experimental values of R_c^2 , $Q_{c\tau}^4$ and $H_{c\tau}^6$ in ^{40}Ca , ^{48}Ca and ^{208}Pb . Those from R_c^2 and $Q_{c\tau}^4$ are taken from Ref.[6]⁷. Although there are ambiguities on the experimental values of H_c^6 by both FB- and SOG-analyses, the FB-values are employed for H_c^6 in Table 10, because Ref.[6] has used the

⁷Note that the definition of the values in Table 7 in Ref.[6] is different from that in the present paper. Ref.[6] has determined the accepted value of the moment by the common region between various LSL-values with errors. Table 4 in the present paper follows Ref.[6].

		H_c^6	H_{cp}^6	H_{cn}^6	H_{cn}^6/H_{cp}^6
^{40}Ca	RMF	4.658×10^3	4.839×10^3	1.812×10^2	0.0374
	SMF	4.474×10^3	4.640×10^3	1.661×10^2	0.0358
^{48}Ca	RMF	4.125×10^3	4.616×10^3	4.904×10^2	0.1063
	SMF	4.041×10^3	4.444×10^3	4.034×10^2	0.0908
^{208}Pb	RMF	5.180×10^4	5.457×10^4	2.767×10^3	0.0507
	SMF	5.220×10^4	5.449×10^4	2.285×10^3	0.0419

Table 9: The values of the sixth moments of the nuclear charge(H_c^6), the proton charge(H_{cp}^6), and the neutron charge(H_{cn}^6) distributions calculated in the relativistic(RMF) and the non-relativistic(SMF) framework in ^{40}Ca , ^{48}Ca and ^{208}Pb . They are related as $H_c^6 = H_{cp}^6 - H_{cn}^6$. The mean square radii of the proton distributions in those nuclei are determined by the least-squares method with the experimental values obtained through Fourier-Bessel analyses of the electron scattering data[6]. The numbers are given in units of fm^6 . The last row shows the ratio of H_{cn}^6 to H_{cp}^6 . For the details, see the text.

		^{40}Ca			^{48}Ca			^{208}Pb		
		R_p	R_n	Q_p	R_p	R_n	Q_p	R_p	R_n	Q_p
$H_{c\tau}^6$	RMF	3.307	3.257	3.600	3.355	3.559	3.624	5.471	5.751	5.792
	SMF	3.322	3.283	3.605	3.358	3.493	3.618	5.460	5.623	5.782
$Q_{c\tau}^4$	RMF	3.336	3.268	3.635	3.371	3.582	3.643	5.463	5.734	5.783
		(0.016)	(0.126)	(0.015)	(0.013)	(0.112)	(0.013)	(0.023)	(0.256)	(0.023)
	SMF	3.341	3.300	3.628	3.367	3.505	3.629	5.453	5.614	5.774
		(0.016)	(0.032)	(0.016)	(0.016)	(0.040)	(0.014)	(0.027)	(0.059)	(0.023)
R_c^2	RMF	3.354	—	—	3.382	—	—	5.453	—	—
		(0.010)	—	—	(0.009)	—	—	(0.014)	—	—
	SMF	3.349	—	—	3.372	—	—	5.447	—	—
		(0.010)	—	—	(0.009)	—	—	(0.014)	—	—

Table 10: The results of the least-squares analysis for the moments of the point neutron and proton distributions in ^{40}Ca , ^{48}Ca and ^{208}Pb . The notations for the components of the moments in the second row and the first column are defined in the text, where τ denotes the protons($\tau = p$) and neutrons($\tau = n$). The values of R_p is obtained from the analyses of H_{cp}^6 , Q_{cp}^4 and R_c^2 , while those of Q_p from H_{cp}^6 and Q_{cp}^4 , and R_n from H_{cn}^6 and Q_{cn}^4 . The experimental values to determine the values of $H_{c\tau}^6$, $Q_{c\tau}^4$ and R_c^2 are employed in the Fourier-Bessel-analyses of the electron-scattering cross sections. The numbers in the parentheses denote the error taking account of the experimental one and the standard deviation of the calculated values from the least-squares line[6]. All the numbers are given in units of fm. For details, see the text.

FB-ones for R_c^2 and $Q_{c\tau}^4$, according to the experimental values in Ref.[10]. Since the value of root msr R_p is frequently used in the literature[4], all the values in Table 10 are given in units of fm. The numbers in the parentheses stand for the error taking account of the experimental one and the standard deviation of the calculated values from the least square line[6]. It is seen that the LSL-values in ^{40}Ca and ^{48}Ca decrease from R_c^2 to H_c^6 in the RMF- and SMF- framework, respectively, while those in ^{208}Pb increase inversely. This different behavior between Ca and Pb is due to fact that the predicted values for Pb in Table 9 is smaller than the FB-values, while those for Ca larger, as mentioned on Table 9 before. Thus if the experimental values of H_c^6 are observed with small experimental errors and those of Q_c^4 are determined more precisely, understanding the MF-models would be advanced. The LSL-values of H_p^6 and Q_n^4 estimated from H_c^6 in the previous section are not listed in Table 10, because there are no values from R_c^2 and $Q_{c\tau}^4$ to be compared to.

Table 10 shows that the values of R_p are larger than the those of R_n in ^{40}Ca , yielding the negative values of the neutron-skin thickness, $\delta R = R_n - R_p$, in contrast to the positive ones in ^{48}Ca and ^{208}Pb . Figs. 5 and 7 for the SOG-values also show the same relationship in ^{40}Ca . This fact may be understood qualitatively, according to the constraint of the Hugenholtz-Van Hove(HVH) theorem in the MF-approximation[35, 36, 37], as below.

Ref.[28] has derived the following equations for R_n and R_p of asymmetric semi-infinite nuclear matter on the basis of the HVH theorem,

$$R_n = \sqrt{\frac{3}{5}} \left(\frac{9\pi A}{8} \right)^{1/3} \frac{1}{k_F} \left(1 + \frac{I}{3} \right) \left(1 - \frac{V_c}{12J} + \frac{V_c^2}{72J^2} + \frac{L}{16K} \frac{V_c^2}{J^2} \right), \quad (38)$$

$$R_p = \sqrt{\frac{3}{5}} \left(\frac{9\pi A}{8} \right)^{1/3} \frac{1}{k_F} \left(1 - \frac{I}{3} \right) \left(1 + \frac{V_c}{12J} + \frac{V_c^2}{72J^2} + \frac{L}{16K} \frac{V_c^2}{J^2} \right), \quad (39)$$

where, in addition to the Fermi momentum(k_F) and the asymmetry parameter($I = (N - Z)/A$), $V_c(> 0)$, J , L and K denote the Coulomb energy, the asymmetry-energy coefficient, the slope of the asymmetry energy, and the incompressibility coefficient. respectively. All the values of the right-hand sides of the above equations are given in each RMF- and SMF-model[28]. Eqs.(38) and (39) provide the neutron skin thickness of the matter, $\delta R_M = R_n - R_p$, as

$$\delta R_M = \sqrt{\frac{3}{5}} \frac{2}{3} \left(\frac{9\pi A}{8} \right)^{1/3} \frac{1}{k_F} \left(I - \frac{1}{4} \left(\frac{V_c}{J} \right) + \frac{I}{24} \left(\frac{3L}{2K} + \frac{1}{3} \right) \left(\frac{V_c}{J} \right)^2 \right). \quad (40)$$

The contribution of the third term in the parenthesis to δR_M is less than 10%. The above equation is examined in detail for ^{208}Pb in Ref.[28], but may be useful for rough discussions on medium-heavy nuclei also.

In ^{40}Ca , $I = 0$ implies $\delta R_M < 0$, so that $R_p > R_n$, whereas in nuclei with $N > Z$ like ^{48}Ca and ^{208}Pb , we have $R_n > R_p$, because of $I > V_c/4J$ [28]. This interpretation may also be related to the result that $Q_n^4 < Q_p^4$ in ^{40}Ca , as mentioned before with respect to Figs. 4 and 6.

The correlation between R_c^2 and R_n^2 is not required in the definition of R_c^2 , but Ref.[6] has shown their well-defined LSL in the used models. This fact implies that the correlation between R_p^2 and R_n^2 is constrained by other requirements in the MF-models. One of them may be Eq.(40) which is dominated by the Coulomb- and asymmetry-energy. Hence, when the mean values of R_c^2 and Q_c^4 are almost equal to their experimental values, respectively, the LSL-value of R_n^2 from R_c^2 may be nearly equal to that from Q_c^4 . Indeed, for example, in ^{208}Pb , the $(R_n^2 - R_c^2)$ -correlation provides the $R_{n,\text{LSL}}^2(R_{c,\text{exp}}^2) = 32.752(0.720) \text{ fm}^2$, while the $(R_n^2 - Q_c^4)$ -correlation $R_{n,\text{LSL}}^2(Q_{c,\text{exp}}^4) = 32.964(0.802) \text{ fm}^2$ in the RMF-models[6]. In the SMF-models,

	$H_c^6(\text{Exp})$	Model	H_{cp}^6	H_p^6	Q_p^4	R_p^2	H_{cn}^6	Q_n^4	R_n^2
^{40}Ca	FB	RMF	4.409	3.369	1.679	1.092	1.750	1.568	1.061
	4.234	SMF	4.395	3.360	1.689	1.103	1.616	1.598	1.078
	SOG	RMF	5.581	4.382	1.999	1.182	1.913	1.851	1.148
	5.390	SMF	5.572	4.367	1.986	1.192	1.824	1.873	1.157
^{48}Ca	FB	RMF	4.384	3.310	1.724	1.125	4.707	2.202	1.267
	3.913	SMF	4.367	3.251	1.714	1.127	3.938	2.020	1.220
	SOG	RMF	4.805	3.671	1.839	1.158	5.068	2.441	1.328
	4.299	SMF	4.721	3.605	1.825	1.159	4.229	2.176	1.262
^{208}Pb	FB	RMF	55.75	48.81	11.26	2.994	28.01	14.09	3.307
	52.95	SMF	55.26	48.57	11.17	2.981	23.11	12.83	3.161
	SOG	RMF	55.74	48.80	11.26	2.994	28.01	14.09	3.307
	52.94	SMF	55.25	48.56	11.17	2.981	23.11	12.83	3.161

Table 11: The LSL-values of the components of the sixth moment H_c^6 in ^{40}Ca , ^{48}Ca and ^{208}Pb . The experimental values of $H_c^6(\text{Exp})$ is obtained by the two ways, which are the Fourier-Bessel(FB)- and the sum-of-Gaussians(SOG)-analysis of the electron-scattering cross section[4]. The nuclear models used to estimate the LSL-values are the relativistic (SMF) and non-relativistic(SMF) mean-field ones. The numbers of $H_c^6(\text{Exp})$, H_{cp}^6 and H_p^6 are listed in units of $10^3 \times \text{fm}^6$, while those of H_{cn}^6 in $10^2 \times \text{fm}^6$. The numbers of Q_p^4 and Q_n^4 are given in units of $10^2 \times \text{fm}^4$, while those of R_p^2 and R_n^2 in $10 \times \text{fm}^2$. For details, see the text.

they are $31.382(0.698) \text{ fm}^2$ against $31.507(716) \text{ fm}^2$ [6]. They are within the errors as written in the parentheses[6]. These results shows that the values of R_n^2 determined by other physical quantities like Eq.(40) are assured to be consistent with the one in Q_c^4 in the MF-framework. It is no doubt to have further information on R_n^2 after determining the experimental values of H_c^6 in future.

As shown in Appendix, the experimental values of H_c^6 are not determined by the FB- and SOG-analyses in Ref.[4]. Ref.[10] employed the FB-method also did not provide those values from their experiment. If the FB- and SOG-coefficients in Ref.[4] are used, H_c^6 -values are calculated as in Table 3. Table 11 lists the LSL-values of the components of H_c^6 , in order to show how their values are sensitive to the ways of the analyses. The values of the components in the rows of SOG are taken from the corresponding figures in §4. Those in the FB-rows are obtained by replacing the horizontal lines in the figures by the FB-ones. It is noticeable that the LSL-values of Q_p^4 and R_p^2 in ^{40}Ca are smaller than those in ^{48}Ca in the FB-analysis, while the former are larger than the latter in the SOG-analysis. This result is due to the big difference between the FB- and SOG-values of H_c^6 in ^{40}Ca , as 4.234×10^3 and $5.390 \times 10^3 \text{ fm}^6$, respectively.

Before closing this subsection, there is a comment on the relationship between the LAS in the present paper and that in Refs.[38, 39, 40] by JLab. They have analyzed the cross sections for the parity-violating electron scattering(PVES) observed at $q = 0.8733 \text{ fm}^{-1}$ in ^{48}Ca and at 0.476 and 0.398 fm^{-1} in ^{208}Pb , q being the momentum transfer from the electron to the nucleus. On the one hand, Table 4 lists the values of $\delta R = R_n - R_p$ in the present method, as $0.220(0.062)$ in the RMF-framework and $0.121(0.036) \text{ fm}$ in the SMF-one for ^{48}Ca , while $0.275(0.070)$ in the RMF-framework and $0.162(0.068) \text{ fm}$ in the SMF-one for ^{208}Pb . On the other hand, Ref.[40] has obtained $\delta R = 0.121(0.050)$ for ^{48}Ca , and Ref.[39] $0.283(0.071) \text{ fm}$ for ^{208}Pb , in the set including the both RMF- and SMF-models. These values are all within the errors in each nucleus, in spite

of the fact that the present LSA is on the moments of the charge distribution observed in the conventional electron scattering[4, 10], while JLab has analyzed the parity-violating asymmetry in the elastic scattering of the polarized electrons from nuclei. Moreover, the LSAs used in the present paper and Refs.[38, 39, 40] are different from each other. For understanding the difference, it is helpful to apply their method for the conventional electron scattering, as follows.

In the present LSA, it is essential to have the reference formula, like Eqs.(10) and (16), which shows the linear relationship between $R_c^{(n)}$ and their components. The LSAs are performed, according to those reference formulae, and the correlations revealed by the LSLs are understood. When the LSA similar to that of JLab is applied for the conventional electron scattering, there is not such a formula between $R_c^{(n)}$ and the cross section. The phase-shift calculations can not decompose the cross section into those from $R_c^{(n)}$, much less into those from $R_\tau^{(m)}$. Nevertheless, the regression equation for the set of the MF-models has to be assumed for the LSA as

$$\sigma(q) = a_q^{(n)} R_c^{(n)} + b_q^{(n)}, \quad (41)$$

where $a_q^{(n)}$ and $b_q^{(n)}$ denote the slope and the intercept of the equation, respectively. Then, Eq.(41) provides the equation in the same way as for Eq.(31),

$$R_{c,\text{LSL}}^{(n)}(\sigma(q)_{\text{exp}}) = \langle R_c^{(n)} \rangle + \frac{1}{a_q^{(n)}} (\sigma(q)_{\text{exp}} - \langle \sigma(q) \rangle). \quad (42)$$

Note that Eq.(42) does not imply

$$R_{c,\text{LSL}}^{(n)}(\sigma(q)_{\text{exp}}) = R_{c,\text{exp}}^{(n)}, \quad (43)$$

but in assuming the above equality, Eqs.(31) and (42) provide

$$(\sigma(q)_{\text{exp}} - \langle \sigma(q) \rangle) = a_q^{(n)} a_{\tau,m}^{(n)} \left(R_{\tau,\text{LSL}}^{(m)}(R_{c,\text{exp}}^{(n)}) - \langle R_\tau^{(m)} \rangle \right). \quad (44)$$

It is, however, unreasonable that all the value of $R_{\tau,\text{LSL}}^{(m)}(R_{c,\text{exp}}^{(n)})$ is determined for all n by a single experimental value of the cross section at any value of q . This result comes from the assumption in Eq.(41) with no reference formula. Thus, there seems not to be a obvious relationship between the present LSA and that of JLab.

The similarity between the values of δR s in JLab and the present analysis may indicate that Eqs.(41) and (43) hold for the small values of n at low q , although the plane-wave Born approximation to the estimation of the cross section is not appropriate for the present discussions[3, 38]. If Eq.(43) is valid for $n = 2$ and 4, the LSA between $R_\tau^{(m)}(m = 2)$ and $\sigma(q)$ would provide the value of δR . One of the ways to verify Eq.(43) for small values of n in the conventional electron scattering is to explore if the right-hand side of Eq.(42) is q -independent, in addition to the fact that the value of $R_{c,\text{LSL}}^{(n)}(\sigma(q)_{\text{exp}})$ is almost equal to the one of $R_{c,\text{exp}}^{(n)}$ which is known already in other experiments[4, 10]. Eq.(43) is also realized, when the value of $R_{c,\text{exp}}^{(n)}$ is reproduced by the model-set as

$$R_{c,\text{exp}}^{(n)} = \langle R_c^{(n)} \rangle. \quad (45)$$

Here the mean value of $R_c^{(n)}$ is calculated by the charge density:

$$\rho_c(r) = \frac{1}{N} \sum_{i=1}^N \rho_{ci}(r), \quad (46)$$

where $\rho_{ci}(r)$ denotes the charge density calculated with the model i in the set of the N models. If $\rho_c(r)$ reproduces all the values of $R_{c,\text{exp}}^{(n)}$ under consideration, the phase-shift calculation with the use of Eq.(46) is expected to explain the experimental value of the cross section as

$$\sigma(q)_{\text{exp}} = \langle \sigma(q) \rangle. \quad (47)$$

Then, Eq.(45) and (47) in Eq.(42) yield Eq.(43).

Once Eq.(43) is found to be valid for $n = 2$, it would be examined for Q_c^4 , and also the related $R_\tau^{(m)}$ of the point proton and neutron distributions. It is interesting to extend the method to H_c^6 also, for which there is no way to extract the experimental values at present. New accurate experimental data at low q -region $\leq 0.8 \text{ fm}^{-1}$ for ^{48}Ca and $\leq 0.5 \text{ fm}^{-1}$ for ^{208}Pb [5] are desired for these considerations, in addition to the previous ones with higher q [4, 10, 41].

The conventional electron-scattering experiment may be performed much more easily than the time-consuming PVES-experiment. Moreover, in order to see the validity of Eq.(42) only, it is not necessary to determine the absolute values of the cross section which require usually other efforts. Suppose that the cross section observed by experiment, $\sigma(q)_{\text{exp}}$, is proportional to the cross section, $\sigma(q)_{\text{ab}}$, whose absolute value is assumed to be known, as

$$\sigma(q)_{\text{exp}} = c\sigma(q)_{\text{ab}}, \quad (c = \text{constant}). \quad (48)$$

Then, if $R_{c,\text{LSL}}^{(n)}(\sigma(q)_{\text{ab}}) = R_{c,\text{LSL}}^{(n)}(\sigma(q_0)_{\text{ab}})$, Eq.(42) is rewritten in terms of the ratio of the cross sections, $A(q) = \sigma(q)_{\text{exp}}/\sigma(q_0)_{\text{exp}}$, as

$$R_{c,\text{LSL}}^{(n)}(\sigma(q)_{\text{ab}}) = \langle R_c^{(n)} \rangle + \frac{\langle \sigma(q_0) \rangle A(q) - \langle \sigma(q) \rangle}{a_q - a_{q_0} A(q)}, \quad (q_0 \neq q), \quad (49)$$

where q_0 stands for one of the momentum transfer which is arbitrarily chosen, avoiding the region $q_0 \approx q$. When the value of $R_{c,\text{LSL}}^{(n)}(\sigma(q)_{\text{ab}})$ is determined, the constant, c , is given by

$$c = \frac{\langle \sigma(q_0) \rangle - \langle \sigma(q) \rangle + (a_{q_0} - a_q)(R_{c,\text{LSL}}^{(n)}(\sigma(q)_{\text{exp}}) - \langle R_c^{(n)} \rangle)}{\langle \sigma(q_0) \rangle - \langle \sigma(q) \rangle + (a_{q_0} - a_q)(R_{c,\text{LSL}}^{(n)}(\sigma(q)_{\text{ab}}) - \langle R_c^{(n)} \rangle)}. \quad (50)$$

If $R_{c,\text{LSL}}^{(n)}(\sigma(q)_{\text{ab}}) = \langle R_c^{(n)} \rangle$, then Eqs.(49) and (50) provide, respectively,

$$A(q) = \frac{\langle \sigma(q) \rangle}{\langle \sigma(q_0) \rangle} = \frac{\sigma(q)_{\text{exp}}}{\sigma(q_0)_{\text{exp}}}, \quad c = 1 + \frac{(a_{q_0} - a_q)(R_{c,\text{LSL}}^{(n)}(\sigma(q)_{\text{exp}}) - \langle R_c^{(n)} \rangle)}{\langle \sigma(q_0) \rangle - \langle \sigma(q) \rangle}. \quad (51)$$

Eq.(50) gives also $c = 1$ for $R_{c,\text{LSL}}^{(n)}(\sigma(q)_{\text{exp}}) = R_{c,\text{LSL}}^{(n)}(\sigma(q)_{\text{ab}})$, as it should be.

It is noted that if $N \rightarrow \infty$ in Eq.(46), then it would provide the ‘model-independent’ charge density, as far as the moments of the charge density is concerned, but in the model-framework used. The real model-independent densities of the point proton and neutron distributions can not be obtained, because the definition of the moment of the charge distributions in RMF and SMF-frameworks are different from each other. Model-dependent contributions to the charge density from the relativistic effects including spin-orbit densities are different in the two frameworks. As a result, for example, there may remain the 0.1 fm difference between R_τ^2 s of the RMF- and SMF-framework in the LSA[6, 29].

6 Summary

The n th moment of the charge distribution, $R_c^{(n)}$, depends not only on the $m(\leq n)$ th moment of the point proton distribution($R_p^{(m)}$), but also on the $m(\leq (n-2))$ th moment of the point neutron one($R_n^{(m)}$)[5]. The experimental value of $R_c^{(n)}$ is determined through electron scattering where the electromagnetic interaction and reaction mechanism are well understood[2, 3]. It is noticeable that the point neutron distribution is investigated, comparing with same experiment as that for the point proton distribution. Both the point proton and the point neutron distribution are most fundamental quantities for description of nuclei.

In order to decompose the experimental value of $R_c^{(n)}$ into the components, $R_\tau^{(m)}(\tau = p, n)$, it is necessary to use nuclear models. At present, it is not avoidable for most of the investigations on nuclear structure to rely on phenomenological models more or less, and it seems to be difficult to select one definitive model among them. In this paper, the mean-field(MF) models have been utilized. There are three reasons why the MF-models are employed. First, they have played an important role in understanding fundamental properties of nuclei, since the early period of nuclear physics[7]. Second, for at least the last 50 years, it is continued to improve the MF-models in the same framework, aiming to explain various static and dynamical aspects of nuclei[9, 12]. The one is the non-relativistic framework(SMF) based on the work of Vautherin and Brink[22], and the other is the relativistic one(RMF) by Horowitz and Serot[42]. As a result, many models with different phenomenological interactions have been accumulated in the same MF-framework[8, 9]. In the case of the SMF-framework, there are more than 100 types of the models[8]. Third, taking advantage of the abundant accumulation of the elaborate models, the least-squares method(LSA) can be used for estimating each value of $R_\tau^{(m)}$ in the model-framework from the single experimental value, $R_c^{(n)}$, as shown in Eq.(32). The LSA reveals the constraint inherent in the model-framework through the least-squares line(LSL). Although the contributions from the neutrons to $R_c^{(n)}$ are about 5% in Q_c^4 and 10% in H_c^6 , they are not a small amount of the correction for the present sophisticated MF-models and appear clearly in the LSLs[6].

The estimated results of $R_\tau^{(m)}$ are summarized in Table 10, where the values of $R_\tau^{(m)}$ related to the sixth moment(H_c^6) of the charge distribution obtained in the present paper are listed, in addition to those from the second(R_c^2) and the fourth moment(Q_c^4) in Ref.[6]. The values from H_c^6 , however, are shown for reference, because their experimental values has not been determined by the Fourier-Bessel- and sum-of-Gaussians-coefficients listed in Ref.[4], as discussed in Appendix. Since higher moments receive more contributions from the neutrons, new methods to determine their experimental values are desired for investigating the moments of the point neutron distribution in detail. In addition, information on higher moments would improve our understanding structure of the nuclear surface.

Finally, one comment is added on the MF-models. It may be continued to improve the MF-models from now on, because there is no basic principle to determine the interaction parameters. For example, no-sea-approximation in the RMF-models neglect the divergence problem due to nucleon-antinucleon states[43, 44]. Those excitations strongly affect the value of the incompressibility(K)[45] which is frequently used as an input-quantity in the RMF-models[9]. The neglect of the divergence terms changes the attractive interaction due to the σ -exchange to the repulsive one unphysically[34]. Moreover, the neglect leads to the violation of the energy-weighted sum rule in the RPA[33]. A proper treatment of the divergence may require additional interaction-parameters in the RMF-models in future. In the non-relativistic models, the effec-

tive mass is determined by the zero-range interactions with the momentum-dependence [12]. Their parameters are related to the enhancement factor κ of the sum of the dipole excitation strengths[46]. The value of κ observed in photo-excitations are mainly due to charge-exchange interactions with finite range[7, 32]. It is not clear, however, how many % of the value of κ should be explained by the momentum-dependent zero-range forces[7, 32]. Moreover, the momentum-dependent zero-range forces may include the finite range effects without charge exchange operators[32]. Thus, there seems to have possibility to require additional parameters in both the RMF- and SMF-models for improvement. In constructing a new MF-model, the LSL and LSL-values obtained in this paper may offer a guide for reproducing the moments, where it is enough to take care of the LSL-values of $R_\tau^{(m)}$ s of the point neutron and proton distributions in each framework, instead of the experimental values of $R_c^{(n)}$ s with complicated corrections.

Acknowledgments

The author would like to thank Professor H. Kurasawa and Professor T. Suda for useful discussions. Most of the numerical calculations are indebted to them. This work was supported by JSPS KAKENHI Grant Numbers JP22K18706.

Appendix

A. Sum rule

Eq.(24) is derived, assuming Eq.(21). More exact derivation of the sum rule is provided as follows. For the LSL-equation:

$$R_c^{(n)} = a_{\tau,m}^{(n)} R_\tau^{(m)} + b_{\tau,m}^{(n)}, \quad (\text{A.1})$$

the element $(R_{\tau,i}^{(m)}, R_{c,i}^{(n)})$ by the model i satisfies

$$R_{c,i}^{(n)} = a_{\tau,m}^{(n)} R_{\tau,i}^{(m)} + b_{\tau,m}^{(n)} + \delta_{\tau,i}^{(m,n)}, \quad (\text{A.2})$$

and by the definition of LSL, their mean values is given by Eq.(18) as

$$\langle R_c^{(n)} \rangle = a_{\tau,m}^{(n)} \langle R_\tau^{(m)} \rangle + b_{\tau,m}^{(n)}, \quad (\text{A.3})$$

where $\delta_{\tau,i}^{(m,n)}$ stand for the deviation from the LSL. The above two equations yield

$$R_{\tau,i}^{(m)} - \langle R_\tau^{(m)} \rangle = \frac{R_{c,i}^{(n)} - \langle R_c^{(n)} \rangle}{a_{\tau,m}^{(n)}} \left(1 - \frac{\delta_{\tau,i}^{(m,n)}}{R_{c,i}^{(n)} - \langle R_c^{(n)} \rangle} \right). \quad (\text{A.4})$$

In the same way, one has for the spin-orbit density

$$W_{\tau,i}^{(n,m)} - \langle W_\tau^{(n,m)} \rangle = \frac{R_{c,i}^{(n)} - \langle R_c^{(n)} \rangle}{a_{W_\tau,m}^{(n)}} \left(1 - \frac{\delta_{W_\tau,i}^{(m,n)}}{R_{c,i}^{(n)} - \langle R_c^{(n)} \rangle} \right) \quad (\text{A.5})$$

with the deviation from the LSL by $\delta_{W_\tau,i}^{(m,n)}$.

Now, according to the definition, $R_{c,i}^{(n)}$ is provided by

$$R_{c,i}^{(n)} = \sum_{\tau,m} \alpha_{\tau,m}^{(n)} R_{\tau,i}^{(m)} + \sum_{\tau,m} W_{\tau,i}^{(n,m)} + C^{(n)}, \quad (\text{A.6})$$

and Eq.(22) holds as

$$\langle R_c^{(n)} \rangle = \sum_{\tau,m} \alpha_{\tau,m}^{(n)} \langle R_\tau^{(m)} \rangle + \sum_{\tau,m} \langle W_\tau^{(n,m)} \rangle + C^{(n)}. \quad (\text{A.7})$$

^{40}Ca	R_c^2	Q_c^4	H_c^6	$\langle r^8 \rangle_c$	^{48}Ca	R_c^2	Q_c^4	H_c^6	$\langle r^8 \rangle_c$
NL3	12.06 (3.473)	209.9 (3.806)	4818 (4.110)	142700 (4.409)	NL3	11.89 (3.448)	196.7 (3.745)	4101 (4.001)	103600 (4.236)
FB	11.90 (3.450)	200.0 (3.761)	4234 (4.022)	106900 (4.252)	FB	11.91 (3.451)	194.7 (3.735)	3913 (3.970)	91690 (4.171)
SOG	12.11 (3.480)	216.5 (3.836)	5390 (4.187)	189300 (4.567)	SOG	11.97 (3.460)	200.5 (3.763)	4299 (4.032)	116100 (4.296)
Ratio	0.9914	0.9804	0.9606	0.9310	Ratio	0.9974	0.9926	0.9846	0.9709

Table 12: The values of the moments of the charge densities in ^{40}Ca and ^{48}Ca calculated by the relativistic mean-field model(NL3[9]) and by the Fourier-Bessel(FB)- and sum-of-Gaussians(SOG)-analyses of electron-scattering data[4]. The numbers of R_c , Q_c , H_c and the eighth root of $\langle r^8 \rangle_c$ are given in units of fm in the parentheses. The last row shows the ratio of the FB-number to the SOG-one in the parentheses. For the notations and details, see the text.

Then, the above two equations give

$$R_{c,i}^{(n)} - \langle R_c^{(n)} \rangle = \sum_{\tau,m} \alpha_{\tau,m}^{(n)} \left(R_{\tau,i}^{(m)} - \langle R_{\tau}^{(m)} \rangle \right) + \sum_{\tau,m} \left(W_{\tau,i}^{(n,m)} - \langle W_{\tau,i}^{(n,m)} \rangle \right). \quad (\text{A.8})$$

Inserting Eqs.(A.4) and(A.5) into Eq.(A.8), finally, the sum rule on the slopes of the LSL-equations is written as

$$1 = \sum_{\tau,m} \frac{\alpha_{\tau,m}^{(n)}}{a_{\tau,m}^{(n)}} \left(1 - \frac{\delta_{\tau,i}^{(m,n)}}{R_{c,i}^{(n)} - \langle R_c^{(n)} \rangle} \right) + \sum_{\tau,m} \frac{1}{a_{W_{\tau,m}}^{(n)}} \left(1 - \frac{\delta_{W_{\tau,i}}^{(m,n)}}{R_{c,i}^{(n)} - \langle R_c^{(n)} \rangle} \right). \quad (\text{A.9})$$

Thus, Eq.(24) is obtained, when $\delta_{\tau,i}^{(m,n)}, \delta_{W_{\tau,i}}^{(m,n)}, \ll (R_{c,i}^{(n)} - \langle R_c^{(n)} \rangle)$. Eq.(A.9) implies that Eq.(32) is also affected by $\delta_{\tau,i}^{(m,n)}$ and $\delta_{W_{\tau,i}}^{(m,n)}$.

B. Fourier-Bessel and Sum-of-Gaussians analyses

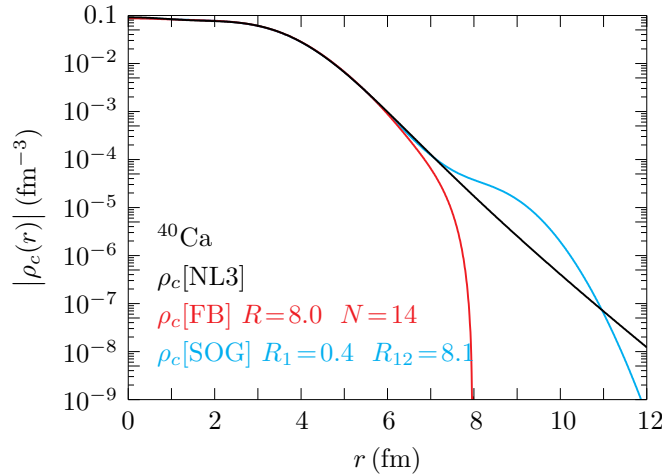


Figure 20: The charge density of ^{40}Ca . The red and blue curves are obtained by the Fourier-Bessel(FB)- and sum-of Gaussians(SOG)-analyses of electron-scattering data, respectively. The black one is calculated using the relativistic mean-field model, NL3. The FB- and SOG-coefficients are taken from Ref.[4]. In the figure, $R = 8$ fm indicates the cut-off parameter, and $N = 14$ the number of the coefficients in FB-series expansion, while the values of R_1 and R_{12} stand for the Gaussian-parameters in Ref.[4]. For details, see the text.

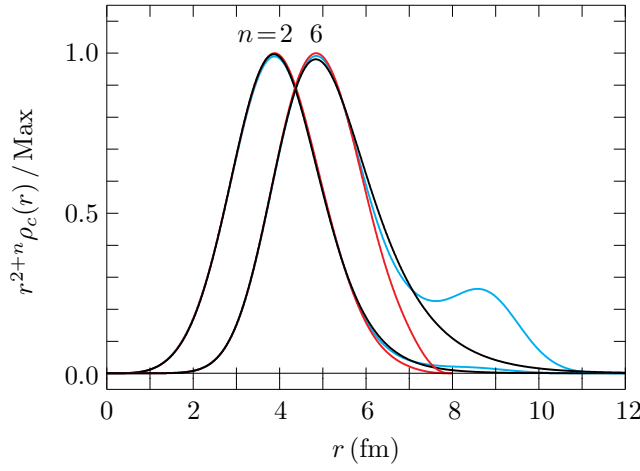


Figure 21: The charge density multiplied r^{2+n} in ^{40}Ca . The charge density is obtained by the Fourier-Bessel(FB)- and sum-of Gaussians(SOG)-analyses of electron scattering data, as in Fig 20. The curves are normalized by the maximum value(Max) of each function. For details, see the text.

It is well known that for analyzing experimental cross section in electron scattering, there are methods which are called “model-independent” ways. The one is Fourier-Bessel(FB)-method[47], and the other sum-of-Gaussians(SOG)-method[48]. In these cases, however, “model-independent” means the analysis to provide charge distribution which fits the experimental cross section without regard to its special functional form like Fermi-type[49]. In fact, the FB-method can not use the infinite series for the analysis, while the SOG-one assumes a finite number of the Gaussian distribution of the fractional charge in the nucleus. Strictly speaking, these analyses imply that if experimental data to be analyzed by FB-method are given by different momentum-transfer regions from those by the SOG-one, then the obtained charge distributions may be different from each other. In principle, in order to determine uniquely the density distribution from experiment, an infinite number of data may be required. Hence, it is necessary to know whether or not the experimental values obtained from these “model-independent” analyses are appropriate for the present purpose.

In this Appendix, the problem of the FB- and SOG-methods is pointed out, which may be avoidable at present for the study of the moments higher than the fourth. Fig. 20 shows the charge density in ^{40}Ca , using the FB(red curve)- and SOG(blue curve)-parameters listed in Ref.[4]. As a reference, the charge density calculated with NL3[9] is depicted with the black curve. According to Ref.[4], the cutoff radius(R) of the FB-series is taken to be 8 fm, while the number of the terms $N = 14$. The numbers, R_1 and R_{12} , indicate examples of the Gaussian-parameters specified in Ref.[4]. Fig. 21 shows the charge density of Fig. 20 multiplied by r^{2+n} ($n = 2, 6$), where the curves are normalized by the maximum value(Max) of each function.

With respect to the values of R_c^2 and Q_c^4 of the charge distribution, there is not a large difference between the two analyses, as listed in Table 12. The SOG-values are obtained with the upper limit of the integral for the moments to be 20 fm. Ref.[4] listed the same values of R_c for ^{40}Ca , as 3.450(10) and 3.480(3) fm in FB- and SOG-analyses, respectively. The values in the NL3 model[9] and those of $\langle r^8 \rangle_c$ are also listed in Table 12, as a reference.

Figures 22 and 23 show the charge density and the one multiplied by r^{2+n} in ^{48}Ca , respectively, in the same way as the previous figures for ^{40}Ca . The dashed parts of FB(red)- and NL3(black)-curves in Fig. 22 indicate the negative densities. The obtained values of R_c for ^{48}Ca are listed in Table 12, which are the same as those in Ref.[4], as

3.451(9) and 3.460(0) fm by the FB- and SOG-analyses, respectively.

Even taking account of experimental errors in the parentheses, in both ^{40}Ca and ^{48}Ca , the values of R_c^2 by the SOG-method are a little larger than those by the FB-one. Their ratio is listed in the last column of Table 12. In the present paper, the experimental and model-dependent errors in the FB- and SOG-analyses were not estimated, because there are not enough data in Ref.[4] for their evaluations. The reason why the SOG-values are larger than the FB-values is easily seen in Figs. 20 to 23. On the one hand, in the SOG-result, there is non-negligible contribution from the tail of the charge density to the R_c^2 , but its contribution depends on the unphysical bump around $r \geq 8$ fm. On the other hand, in the FB-one, the cutoff parameter, $R = 8$ fm, dominates the shape of the density-tail. In particular, in ^{48}Ca , the negative density appears owing to series of the spherical Bessel functions, whereas that of NL3 around $r = 11$ fm is due to the neutron charge density. The SOG-components are not negative by definition.

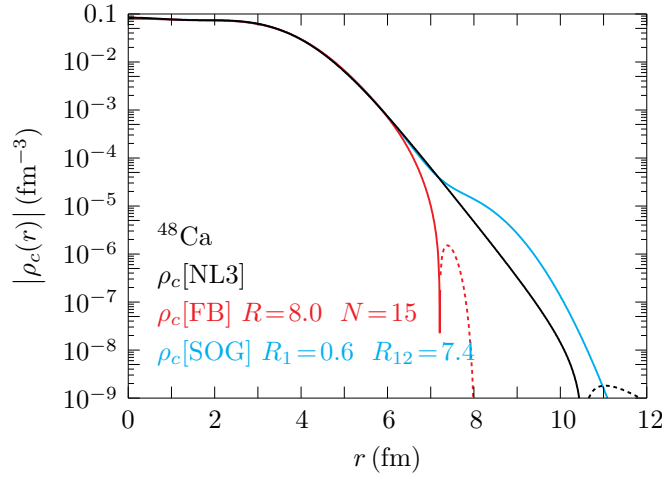


Figure 22: The charge density of ^{48}Ca . The figure is depicted in the same way as Fig. 20, but the dashed parts of red and black curves indicate the negative densities. The FB- and SOG-coefficients are taken from Ref.[4]. For details, see the text.

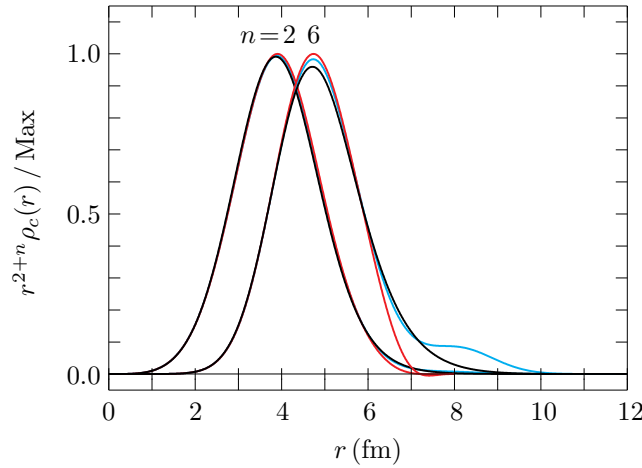


Figure 23: The charge density multiplied r^{2+n} in ^{48}Ca . The figure is depicted in the same way as Fig. 21. For details, see the text.

Figures 24 and 25 are the same as Figs. 20 and 21, but for ^{208}Pb . Ref.[4] listed in the FB-method the two different values of R_c in ^{208}Pb for the two corresponding sets of experimental data. The one was obtained with $R = 12.0$ fm, while the other $R = 11.0$ fm. The former, which is used in the present paper, has 17 coefficients of FB-series, yielding

$R_c = 5.503(2)$. The latter has 13 ones and provides $R_c = 5.499(1)$.

In the FB-analysis, the oscillation of the charge density is observed, whereas in the SOG-one, the density decreases monotonically with r up to 20 fm. As a results, the ratio of the FB-value to the SOG-one is 1.0000 for R_c , Q_c and H_c in ^{208}Pb , as expected from Fig. 25. The obtained values are $Q_c = 5.851$ and $H_c = 6.128$ fm, and the value of R_c is the same as 5.503 fm listed in Ref.[4].

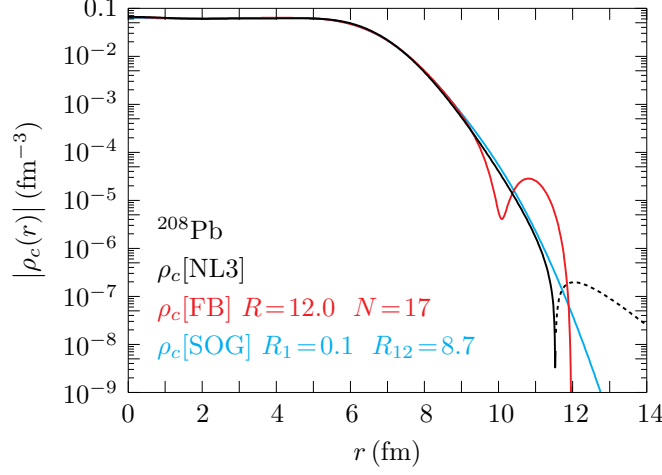


Figure 24: The charge density of ^{208}Pb . The figure is depicted in the same way as Fig. 20, but the dashed parts of red and black curves indicate the negative densities. The FB- and SOG-coefficients are taken from Ref.[4]. For details, see the text.

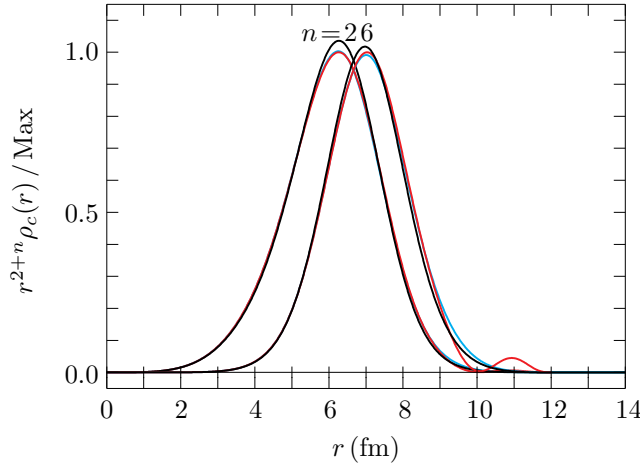


Figure 25: The charge density multiplied r^{2+n} in ^{208}Pb . The figure is depicted in the same way as Fig. 21. For details, see the text.

Calculations of R_c in an accuracy within 1%[50] should take care of the problems of the density-tails in the FB- and SOG-analyses, but a few % difference is not essential for the present discussions. In the discussions on H_c^6 in the present paper, however, the difference between the FB- and SOG-values are not disregarded, because of the two reasons. The one is that the cutoff radius $R = 8$ fm for ^{40}Ca and ^{48}Ca in the FB-analyses seems not to be enough for covering most of the region where the function $r^8\rho_c(r)$ is finite, as seen in Figs. 21 and 23. In the FB-analysis, the value of the n th moment is proportional to R^n . In SOG-calculations, the cut-off radius is required to be at least 12 fm for the enough convergence of the integral on H_c^6 . The other reason is that the unphysical negative density in FB-distribution and the bump in SOG-one contribute to the values of H_c^6 , as seen in Figs. 21, 23 and 25. Since there are not enough experimental data to improve

the results of Ref.[4] at present, the LSA of H_c^6 has been performed by using the both FB- and SOG-values, but in §4 the LSA has been shown by using the values of the SOG-method. The results with the FB-values will be summarized in §6, together with those of the SOG-one. It is noted that Table 12 shows the worst ratio of the FB-value to the SOG-one is 0.9606 for H_c in ^{40}Ca among the moments discussed in the present paper.⁸

References

- [1] M. Thiel et al., J. Phys. G : Nucl. Part. Phys. **46**, 093003 (2019).
- [2] J. D. Bjorken and S. D. Drell, Relativistic quantum mechanics (McGraw Hill Book Company, 1964).
- [3] T. deForest and J. D. Walecka, Adv. Phys. **15**, 1 (1966).
- [4] H. De Vries C. W. De Jager and C. De Vries, Atom. Data Nucl.Data Tabl. **36**, 495 (1987).
- [5] H.kurasawa and T. Suzuki, Prog. Theor. Exp. Phys. **2019**, 113D01 (2019).
- [6] H. Kurasawa, T. Suda and T. Suzuki, Prog. Theor. Exp. Phys. **2021**, 013D02(2021).
- [7] A. Bohr and B. R. Mottelson, Nuclear structure, vol.1 (World Scientific Publishing Co. Pte. Ltd., 1998).
- [8] J. R. Stone et al., Phys.Rev. **C68**, 034324 (2003).
- [9] G. A. Lalazissis, J. Köning and P. Ring, Phys. Rev. **C55**, 540 (1997).
- [10] H. J. Emrich, PhD thesis, Johannes-Gutenberg-Universität, Mainz,1983.
- [11] M. M. Shama, M. A. Nagarajan, and P. Ring, Phys. Lett. **B312**, 377 (1993).
- [12] E. Chabanat, et al., Nucl. Phys. **A635**, 231 (1998).
- [13] H. Kurasawa and T. Suzuki, Phys. Rev. **C62**, 054303 (2000).
- [14] D. Vretenar, T. Nikšić and P. Ring, Phys.Rev. **C68**, 024310 (2003).
- [15] B. D. Serot and J. D. Walecka, Int. Jour. Mod. Phys. **E6**, 515 (1997).
- [16] P. G. Reinhard et al., Z. Phys **A323**, 13 (1986).
- [17] M. Rufa et al., Phys. Rev. **C38**, 390 (1988).
- [18] P. G. Reinhard, Z. Phys. **A329**, 257(1988).
- [19] G. A. Lalazissis, J. König, and P. Ring, Phys. Rev. **C55**, 540 (1997).
- [20] Y. Sugahara and H. Toki, Nucl. Phys. **A579**, 557 (1994).
- [21] B. G. Todd-Rutel and J. Piekarewicz, Phys. Rev. Lett. **95**, 122501(2005).
- [22] D. Vautherin and D. M. Brink, Phys. Rev. **C5**, 626 (1972).
- [23] M. Beiner et al., Nucl. Phys.**A238**, 29 (1975).
- [24] J. Bartel et al., Nucl. Phys. **A386**, 79 (1982).

⁸The oscillations in the densities obtained by the FB- and SOG-methods have been pointed out in Ref.[51] also.

- [25] E. Chabanat et al., Nucl. Phys. **A627**, 710 (1997)
- [26] N. V. Giai and H. Sagawa, Phys. Lett. **B106**, 379 (1981).
- [27] H. S. Köhler, Nucl. Phys. **A258**, 301 (1976).
- [28] T. Suzuki, Prog. Theor. Exp. Phys. **2022**, 063D01 (2022).
- [29] H. Kurasawa and T. Suzuki, Prog. Theor. Exp. Phys. **2022**, 023D03 (2022).
- [30] X. Roca-Mazza, M. Centelles, X. Viñas and M. Warda, Phys. Rev. Lett., **106**, 252501 (2011).
- [31] D. J. Thouless, Nucl. Phys. **22**, 78 (1961).
- [32] T. Suzuki, Ann. de Phys. Fr., **9**, 535 (1984).
- [33] H. Kurasawa and T. Suzuki, Prog. Theor. Exp. Phys., **2013**, 043D04 (2013).
- [34] H. Kurasawa and T. Suzuki, Prog. Theor. Exp. Phys., **2015**, 113D02 (2015).
- [35] H. A. Bethe, Phys. Rev. **103**, 1353 (1956).
- [36] V. F. Weisskopf, Nucl. Phys. **3**, 423 (1957).
- [37] N. M. Hugenholtz and L. Van Hove, Physica **24**, 363 (1958).
- [38] S. Abrahamyan et al., Phys. Rev. Lett. **108**, 112502 (2012).
- [39] D. Adhikari et al., Phys. Rev Lett. **126**, 172502 (2021).
- [40] D. Adhikari et al., Phys. Rev Lett. **129**, 042501 (2022).
- [41] R. F. Frosch, et al., Phys. Rev. **174**, 1380 (1968).
- [42] C. J. Horowitz and B. D. Serot, Nucl. Phys. **A368**, 503 (1981).
- [43] J. F. Dawson and R. J. Furnstahl, Phys. Rev. **C42**, 2009 (1990).
- [44] Z. Ma, N. Van Giai, A. Wandelt, D. Vretenar, and P. Ring, Nucl. Phys. **A686**, 173 (2001).
- [45] H. Kurasawa and T. Suzuki, Phys. Lett. **B474**, 262 (2000).
- [46] E. Chabanat, et al., Nucl. Phys. **A627**, 710 (1997).
- [47] B. Dreher, et al. Nucl. Phys. **A235**, 219 (1974).
- [48] I. Sick, Nucl. Phys. **A218**, 509 (1974).
- [49] J. Friedrich and F. Lenz, Nucl. Phys. **183**, 523 (1972)
- [50] G. Hargen et al., Nature Phys. **12**, 186 (2016).
- [51] L. Xayavong and Y. Lim, Arxiv-nucl-th, 2303.00945 (2023).